Studies of the Ferromagnetic Superconductors URhGe and UCoGe

Studies of the Ferromagnetic Superconductors URhGe and UCoGe

By
Travis J. Williams, B.Sc.

A Thesis
Submitted to the School of Graduate Studies
in Partial Fulfilment of the Requirements
for the degree of
Master of Science

McMaster University

MASTER OF SCIENCE (2009) McMaster University
(Department of Physics and Astronomy) Hamilton, Ontario

TITLE: Studies of the Ferromagnetic Superconductors URhGe and UCoGe

AUTHOR: Travis J. Williams, B.Sc.
SUPERVISOR: Dr. Graeme M. Luke

NUMBER OF PAGES: *xvii*, 82

Abstract

This thesis comprises studies on two ferromagnetic superconductors, URhGe (T_{Curie}=9.5K and T_{SC}=250mK) and UCoGe (T_{Curie}=2.5K and T_{SC}=800mK). These properties are interesting because the current theory to explain superconductivity predicts that ferromagnetism should destroy superconductivity. Not only is that not true in these materials, but ferromagnetism and superconductivity are thought to arise from a common mechanism. The studies conducted on these materials arise from that possibility, in an attempt to understand the unconventional nature of these materials.

Original work is contained in chapters 4, 5 and 6. All of this work is currently not published in sources other than this thesis.

Chapter 1 will give an introduction to these materials, and the work that has been done on them by other groups, and work done on related materials.

Chapter 2 will give details of the various experimental methods used in measuring the structure and properties of the materials studied. This work was conducted by the author at McMaster University, with the assistance of individuals from the Brockhouse Institute for Materials Research, and the Center for Electron Microscopy at McMaster University.

Chapter 3 will provide an introduction to the technique of muon Spin Resonance/Relaxation (μSR). This work was done at the TRIUMF facility in Vancouver, British Columbia, with the assistance of several TRIUMF staff. The data was collected by the author, and other members of Dr. Luke's research group as well as

collaborators from TRIUMF and from Columbia University.

Chapter 4 will present the measurements made on UCoGe, while Chapter 5 presents the measurements of URhGe. Details of the crystal growth and structure characterization measurements are included in these chapters, along with resistivity, bulk magnetization and μSR measurements.

Both zero-field (ZF) and transverse field (TF) μSR has been performed. This work focuses on studying the magnetic moment size, and the magnetic volume fraction around the ferromagnetic transition, and to temperatures as low as 20mK. Consideration is also given to the magnetic and superconducting properties in the low-temperature region.

In the Introduction, URhGe is presented first, followed by UCoGe, since this was the order in which they were discovered. The results obtained from UCoGe are presented first, since work on that compound was started before the work on URhGe.

Chapter 6 focuses on the conclusions drawn from this work, comparing the measurements of both materials.

Keywords: muon spin rotation, ferromagnetism, superconductivity, heavy fermions.

Acknowledgements

My foremost thanks goes to my supervisor, Dr. Graeme Luke. The two years spent with him and his family have been a great experience both professionally and personally. I know that my experience and my growth as a graduate student owes more to Graeme than to anyone else, and for this I am extremely grateful. I know that he has provided a great role model for me as I continue to become a professional in this field.

I also need to acknowledge the great support I have received from other members of Dr. Luke's research group, current and former: Adam Aczel, Greg MacDougall, Jose Rodriguez, and Weiqiang Yu. The time that they spent to help me with running and analyzing my experiments has been invaluable.

In addition to these individuals, various institutions and their staff have contributed to my work, to whom I owe thanks: our collaborators at Columbia University who conduct μSR experiments with us, Dr. Yokotomu Uemura and Jeremy Carlo; Dr. Tatsuo Goko and other TRIUMF staff for their help with the μSR measurements and instrumentation; and at BIMR, Jim Garrett, Paul Dube and Dr. Steve Koprich for their help with crystal growth, SQUID and SEM measurements respectively.

I have also been fortunate to have been able to share professionally and personally with many members of the McMaster Department of Physics and Astronomy faculty, staff and students. They have provided more than a work environment; the Department has become a place that I look forward to spending my time, and will continue to consider a home-away-from-home. A few members of the Department to whom I owe a special

gratitude are faculty members Dr. Bruce Gaulin and Dr. Takashi Imai, who have both proven to be a great asset. I would also like to thank Dr. Kari Dalnoki-Veress for taking such a personal interest in my graduate experience; it has made the time spent in the Department easier, more enjoyable, and more fulfilling. There are several students outside of my research group that I am fortunate to count as both colleagues and friends: Patrick Clancy, Fanlong Ning, Clare Armstrong, Greg Van Gastel, Greg Egan, as well as the other members of Dr. Gaulin's, Dr. Imai's, and Dr. Timusk's research groups. I'm very glad to have their support in my research, my academics, and my life outside of work.

I am further blessed to have a wonderfully supportive family. My parents, Terry and Margaret Williams have been ever-supportive of my love of physics, always offering to help even when they profess not to know anything about what I am doing. Secretly, I think they know more than they let on, and are just showing me that they are always there for me. My brother, Cameron, has also been both inspirational and supportive. I have come to rely on him to keep me sane and in touch with reality on many occasions.

Finally, my greatest source of both motivation and encouragement has been my amazing girlfriend, Kelly. Without her, I would never have stayed sane, focused, and determined in this project. Her love and support has meant more to me than I could express, and I am truly blessed to have someone so wonderful behind me. Kelly, thank you for everything. I love you.

Table of Contents

Abstract. . . . . *iii*

Acknowledgements. . . . . *v*

List of Figures. . . . . *ix*

List of Tables . . . . . *xvi*

I. Introduction 1

1.1 Heavy Fermion Materials. 1

1.2 Heavy Fermion Superconductivity 4

1.3 Ferromagnetism and Superconductivity. 7

1.4 URhGe 9

1.5 UCoGe 13

II. Experimental Methods 16

2.1 Crystal Growth 16

2.2 Structure Characterization Techniques. 19

2.3 DC Resistivity 23

2.4 Bulk Magnetometry. 24

III. Muon Spin Relaxation/Rotation. 27

3.1 Principles of μSR 27

3.2 Zero Field μSR 30

3.3 Transverse Field μSR 33

IV. Measurements of UCoGe 34

4.1 Structure Characterization. 34

4.2 DC Resistivity 39

4.3 Bulk Magnetometry. 42

4.4 μSR 46

4.5 Conclusions. 53

V. Measurements of URhGe 55

5.1 Structure Characterization. 55

5.2 DC Resistivity 61

5.3 Bulk Magnetometry. 63

5.4 μSR 65

5.5 Conclusions. 70

VI. Conclusions 72

6.1 Structure Characterization. 72

6.2 DC Resistivity 73

6.3 Bulk Magnetometry 74

6.4 μSR 75

6.5 Conclusions 76

References 78

List of Figures

Figure # **Page**

1.1 Phase Diagram of UGe_2 8

Temperature-pressure phase diagram of UGe_2. The superconducting transition, T_{SC}, is taken from a 50% drop resistivity. Lines are only a guide to the eye. Figure taken from [32].

1.2 URhGe Structure. 10

The orthorhombic TiNiSi structure of URhGe. This structure is present at all temperatures. Figure taken from [35].

1.3 URhGe Pressure-Temperature Phase Diagram. 12

Pressure-temperature phase diagram of URhGe. This shows an increase in T_{Curie} with applied pressure, and a critical pressure for superconductivity at 4.1GPa. Figure taken from [42].

1.4 URhGe Field-Temperature Phase Diagram 12

Magnetic field-temperature phase diagram of URhGe. The field was applied along the b *axis. This shows a critical field around 2T, and reentrant superconductivity between 8 and 12.5T. Figure taken from [39].*

1.5 UCoGe Pressure-Temperature Phase Diagram. 14

Pressure-temperature phase diagram of UCoGe. This shows an decrease in T_{Curie} with applied pressure. Figure taken from [46].

2.1 Schematic of Mono-Arc Furnace 16

Schematic of a mono-arc furnace. The sample is placed on the stage, and a high voltage supply creates an arc from the stinger to the sample, heating the sample. The stage is rotated to heat the sample uniformly, and facilitate mixing. The entire setup is enclosed in a glass bulb, back-filled with Ar gas.

2.2 Schematic of Tri-Arc Furnace. 17

Schematic of a tri-arc furnace. The sample is placed on the stage, and a high voltage supply creates an arc from the three stingers to the sample, heating the sample. A seed rod is lowered into contact with the molten sample, then pulled

upwards. The seed rod is cooled with water, so that the sample crystallizes on the seed rod, with the molten sample below. The seed rod and stage are counter-rotated to create a straight crystal. The entire setup is enclosed in a glass bulb, back-filled with Ar gas.

2.3 X-ray Scattering in a Crystal 19

X-ray scattering in a crystal. (a) *Destructive interference. The photons are out of phase, and they cancel.* (b) *Constructive interference. The photons are in phase, and they interfere constructively.*

2.4 Example of a Laue Diffraction Image 21

Example of a Laue diffraction pattern. This pattern was obtained from a single crystal of La_2CuO_4. The high symmetry point near the centre is one of the major axes.

2.5 Example of a Powder X-ray Diffraction Image 22

Example of a powder X-ray diffraction pattern. The upper set of peaks is the measured data. The vertical lines indicate the position of the Bragg peaks. The line at the bottom is the difference between the measured and calculated values, based on the calculated structure. Figure taken from [56].

2.6 Schematic of a Four-point Resistance Measurement 23

Schematic representation of a four-point resistance measurement. This method isolates the sample resistance from the resistance of the components.

2.7 Schematic of the SQUID Magnetometer 25

Schematic representation of the SQUID magnetometer. The inset shows the sample space and the four pickup coils. Figure taken from [59].

3.1 Probability distribution of Positron momentum, produced from Muon decay. . .29

Representation of the probability distribution of the positron momentum produced from muon decay (Equation 3.6). This distribution is calculated from the function given in Equation 3.7. Figure taken from [59].

3.2 Experimental Geometry of a Zero-Field (ZF) μSR Experiment 31

The experimental geometry of a ZF- μSR experiment. Here, we define $\hat{z}$ as being the beam direction, $\hat{y}$ is Up-Down, and $\hat{x}$ is Right-Left Figure taken from [59].

4.1 Powder X-Ray Pattern for the First UCoGe crystal 35

The powder X-ray measurements for the first growth of UCoGe. This is plotted

as a semi-log plot. Several small impurity peaks are seen, particularly around 37°.

4.2 Theoretical Powder X-Ray Pattern for UCoGe 35

The theoretical powder X-ray pattern of UCoGe, based on the data given in [51].

4.3 Laue Diffraction Measurements of the First UCoGe Crystal. 37

A Laue diffraction measurement on the first sample of UCoGe. This shows no obvious high-symmetry points, indicating no dominant grain. The image indicates several grains visible in this area of the crystal. The bright area at the bottom of the image is the sample holder.

4.4 Laue Diffraction Measurements of the Second UCoGe Crystal. 38

The Laue diffraction pattern from Figure 4.4(b) *is fit with orientation software. This pattern is shown again in* (a). (b) *The calculated points given by the fitting software is indicated by red dots at the calculated locations of the Bragg peaks. This is based on the centre of the image being aligned with the a-axis.* (c) *This is the stereoscopic projection of the Bragg peaks based on the fit. This shows the positions of the other major axes.*

4.5 Orientation of the Second UCoGe Crystal from Laue Measurements 38

The Laue diffraction pattern from Figure 4.4(a) *is fit with orientation software. This pattern is shown again in* (a). (b) *The fit given by the orientation software is indicated by red dots at the calculated positions of the Bragg peaks, based on the centre of the image being aligned with the* a-*axis.* (c) *The stereoscopic projection of the Bragg peaks based on the fit. This image also shows the positions of the other major axes.*

4.6 Resistivity of the First UCoGe Crystal. 39

The resistivity of the first UCoGe crystal from 1.7K to 60K. We see a continuous downturn, occurring around 30K.

4.7 Resistivity of the Second UCoGe Crystal. 41

The resistivity of the second UCoGe crystal from 0.02K to 300K. The resistance peaks around 40K, then decreases. The drop below 8K is due to instrumentation. (inset) *The low-T resistance shows the onset of superconductivity at 425mK, and zero resistance below 300mK.*

4.8 Susceptibility of the First UCoGe Crystal 43

Magnetic susceptibility, χ_1, versus temperature for the first UCoGe crystal. A slight downturn is observed below 5K, which may indicate the proximity to a

magnetic transition. The fit to a Curie-Weiss Law gives good agreement to the data, and yields a value of T_{Curie} = 1.98(2)K.

4.9 Hysteresis Loop in the first UCoGe Crystal. 44

Hysteresis loop in the first UCoGe sample, done at T = 1.7K. This loop is slightly open, indicating soft ferromagnetic order.

4.10 Inverse Susceptibility of the Second UCoGe Crystal. 45

Magnetization and U Moment size for the second UCoGe crystal. The upturn indicates the onset of a magnetic transition, though data below 1.7K is needed to fill in this transition. The U moment size is smaller than indicated elsewhere, though the low-T data is needed to find the saturated moment. This was fit to Equation (4.1), giving T_{Curie} = 0.99(3)K.

4.11 ZF-μSR Spectra of the Second UCoGe Sample 47

ZF-μSR spectra of the second UCoGe crystal at 5K and 1K. The spectrum at 5K is characteristic of paramagnetic behaviour, while the lower spectrum is indicative that the sample is in the ferromagnetic state at 1K.

4.12 Fit to the ZF-μSR Spectrum 48

ZF-μSR spectra of the second UCoGe crystal at 1K, 0.5K and 20mK, fit to Equation (4.2). The amplitude of the oscillatory signal decreases in the superconducting region, while the frequency also drops by ~10%.

4.13 Frequency of the ZF-μSR Spectrum 49

Frequency versus temperature in the ZF-μSR spectra of the second UCoGe crystal, from 20mK to 5K. We see that above T_{Curie}, the frequency fits to a value of approximately zero, with an increase to 1.9MHz between 0.5K and 1.5K, characteristic of ferromagnetism. Below T_{SC}, the frequency drops by ~10%.

4.14 Relaxation rate of the ZF-μSR Spectrum 50

ZF-μSR plot of the Relaxation versus Temperature in the second UCoGe crystal. The relaxation rate increases below T_{Curie}, decreases sharply at the superconducting transition, then increases towards T=20mK.

4.15 TF-μSR Spectra of the Second UCoGe Crystal in 200G 51

The TF-μSR spectra of the second UCoGe crystal in an applied field of 200G, shown at 4K (open circles) and 20mK (filled circles). We see an increased relaxation with decreasing temperature.

4.16 Frequency of the TF-μSR Spectrum. 51

TF-μSR plot of Frequency versus Temperature in the second UCoGe crystal. The measurements were done in an applied field of 200G, while cooling the sample in zero applied field. This displays no clear indication of superconductivity.

4.17 Relaxation of the TF-μSR Spectrum. 52

TF-μSR plot of Relaxation versus Temperature in the second UCoGe crystal. The measurements were done in an applied field of 200G, while cooling the sample in zero applied field. From these measurements, T_{Curie} appears to be approximately 2.5K.

5.1 Laue Diffraction Measurements of the First URhGe Crystal. 55

A Laue diffraction measurement on the first sample of URhGe. A symmetry point is visible on the lower left of the image. Some of the points, particularly those above the centre, indicate multiple grains. The bright area in the bottom of the image is the sample holder.

5.2 Laue Diffraction Measurements of the Second URhGe Crystal. 56

The Laue diffraction measurements on the second sample of URhGe. Both image are taken at the terminal end of the growth, at a point where the crystal had broken. (a) *is taken parallel to the growth axis, while* (b) *was taken perpendicular to the broken face. Both images show multiple grains in the crystal.*

5.3 Powder X-Ray Measurements of the Second URhGe Sample. 57

The powder X-ray measurements for the second growth of URhGe. This is plotted as a semi-log plot. Some small impurity peaks are noticeable.

5.4 Theoretical Powder X-Ray Pattern for URhGe 57

The theoretical powder X-ray diffraction pattern for URhGe based on the lattice constants in Table 1.4 and the Wyckoff positions of UCoGe from [51]. This pattern agrees very well with the experimental pattern in Figure 5.3.

5.5 Laue Pattern of the Surface of the Second URhGe Growth. 59

The Laue diffraction measurements on the surface of the first URhGe growth. This clearly shows powder rings, indicating that the surface of the crystals are not crystallographically similar to the interior of the crystal. This prompted the SEM analysis.

5.6 SEM Image of the Second URhGe Growth 60

The SEM image of the surface of the URhGe crystal. There is a second phase on the surface, ~1-2μm thick. This image is approximately 5950x magnification.

5.7 EPMA Measurements of the URhGe Crystal. 60

The EPMA measurements of the bulk and surface of the URhGe crystal. (a) *The bulk spectrum shows the presence of U, Rh and Ge.* (b) *The surface spectrum shows the absence of Rh peaks, and U and Ge in approximately equal amounts.*

5.8 Resistivity of the Second URhGe Crystal 61

The resistivity of the second URhGe crystal from 1.7K to 60K. We see the onset of ferromagnetism at 9.5K. The resistivity follows $\rho \propto T^2$ *below the transition.* (inset) *The resistivity below 10K is plotted against temperature squared, and it can be seen that the resistvity is linear in* T^2.

5.9 Resistivity of the Second URhGe Crystal at low Temperature. 62

The resistivity of the second URhGe crystal from 0.02K to 300K. We see the onset of ferromagnetism at T = 9.5K. Another sharp change is seen at 4.5K, but this is likely due to instrumentation. (inset) *The resistivity of the URhGe crystal below 1.5K. No evidence of superconductivity appears down to 0.02K.*

5.10 Magnetization of the URhGe Crystal. 64

Magnetization and U moment size versus Temperature. A clear ferromagnetic transition is seen at 9.5K, and the moment size agrees fairly well with values reported elsewhere.

5.11 Hysteresis Loop of the Second URhGe Crystal 64

Hysteresis loop of the second URhGe crystal at T = 1.7K. The sample is shown to be magnetically ordered, since hysteresis is present at this temperature. This is expected from the susceptibility measurements.

5.12 ZF-μSR Spectra of the Second URhGe Crystal 66

ZF-μSR spectra of the URhGe crystal at 10.5K and 1.8K. The spectrum at 10.5K is characteristic of paramagnetic behaviour, while the spectrum at 1.8K is indicative that the sample is in the ferromagnetic state.

5.13 Fit to the ZF-μSR Spectrum of URhGe 68

ZF-μSR spectra of the URhGe crystal at 60mK. The solid line shows the fit to the data given by Equation (5.3). The fit to this spectrum had a reduced $\chi^2 = 1.235$, *which was typical for runs below 1.8K.*

5.14 Frequency of the ZF-μSR Measurements in URhGe 68

Frequency of the μSR signal fit using Equation (5.3). This clearly shows no precession above $T_{Curie} = 9.5K$. *The frequency increases toward T = 0K, and*

shows no change at low T.

5.15 Low-Temperature Frequency of URhGe 69

Low temperature frequency of the ZF-μSR signal. The black points are those measured in a 2008 study, while the red points were values that were done in 2009 to check the behaviour. No noticeable changes occur at low T.

List of Tables

Table # **Page**

1.1 Heavy Fermion Ground States and Ordering Temperatures. 3

Ordering temperature of various heavy fermion materials with different ground state configurations. Data taken from [1, 15, 16].

1.2 Properties of Heavy Fermion Superconductors 5

Selected properties of some heavy fermion superconductors at ambient pressure. Values indicated by slashes (\) refer to different crystallographic directions. Dashes (-) indicate a range of measured values. Data taken from [12, 22].

1.3 Heavy Fermion Moment sizes 7

Effective moment sizes of various heavy fermion materials at low temperature.

1.4 URhGe Lattice Constants. 10

The lattice constants of URhGe at ambient pressure. Data taken from [38].

1.5 Comparison of Select Properties of URhGe and UGe_2 11

Comparison of selected properties of URhGe and UGe_2. These properties suggest that URhGe should be in close proximity to a quantum critical point. Data taken from [41].

1.6 UCoGe Lattice Constants. 13

The lattice constants of UCoGe at ambient pressure. Data taken from [45].

I. Introduction

1.1 Heavy Fermion Materials

Heavy fermion systems are a family of strongly-correlated electron materials [1]. These materials are so-named due to the large effective masses of their conduction electrons. This is observed experimentally through large electron contributions to the specific heat at low temperatures [2], and heavy quasiparticles in the de Haas-van Alphen (dHvA) effect [3]. This situation typically arises in *f*-band conduction electrons, so these materials are generally based on intermetallics such as Ce, Yb, and U, though not exclusively [1].

At moderate temperatures ($T > 50K$), these materials act as ordinary paramagnetic metals, with weakly interacting magnetic moments. When the temperature is decreased, the moments located on the *f*-electrons become strongly coupled to each other, and to the conduction electrons [1]. This increases the effective mass of the conduction electrons, to values that are 10 to 100 times the bare electron mass. This mass enhancement is clearly observed in heat capacity [4,5] and de Haas-van Alphen measurements [6].

The transport properties of heavy fermion systems display an usually large amount of variation at low temperatures. Whereas normal metals generally have a nearly constant resistivity below 20K, many heavy fermion systems show rapid variation, and behaviour that is consistent with scattering dominated by magnetic moments [1].

Heavy fermion systems also display some pressure dependence in many of their properties. Many materials that have a non-magnetic ground state will order at a critical pressure [7]. This is thought to be a result of changes in the distance between the moments, which affects the strength of the interactions.

The leading description of the heavy fermion phenomenon is the competition between the Ruderman-Kittel-Kasuya-Yosida (RKKY) interaction and the Kondo Effect. The RKKY interaction is based on the existence of an indirect exchange through the polarization of the conduction electrons [8, 9, 10]. The Kondo effect is an antiferromagnetic exchange interaction between the localized and conduction electrons, leading to the enhancement in the effective mass [11]. This can occur between conduction electrons and a single magnetic impurity, or a lattice of magnetic ions. In the latter case, the lattice of magnetic atoms is called a Kondo lattice. This also appears as a reduction in the effective moment size in the system [12]. In *f*-band intermetallics, these atoms appear as magnetic moments with a large screening cloud, which changes between the high- and low-temperature regime.

The cross-over between these two regions occurs due to a competition between inter- and intra-site interactions. [13]. These interactions are both related through a common exchange coupling between the conduction electrons and local moments [12]. This cross-over appears in transport measurements as a maximum in the resistivity of the material, and indicates a loss in inelastic scattering below the cross-over [12].

The competition between the RKKY and the Kondo interactions depends on the same coupling parameter, since they both involve coupling of the *f*-electron moment and the conduction electrons. While the Kondo effect screens local moments, tending to a non-magnetic state, the RKKY interaction favours long-range magnetic order. This competition results in a phase diagram in which a magnetic region can form for a range of coupling constant values at low temperature, which has been dubbed the Doniach model [14].

This phenomenon leads to materials with many interesting possible ground states, depending mostly on the strength of the interactions. The ground states are usually magnetic (both antiferromagnetic and ferromagnetic have been observed), superconducting, or in some cases, non-magnetic [1]. Table 1.1 shows

some of the heavy-fermion materials, and their ground state.

	Ordering Temperature (K)
Antiferromagnetic	
$UPtGa_5$	27.0
$UAgCu_4$	18.15
URu_2Si_2	17.0
UCu_5	15.2
U_2Zn_{17}	9.7
UCd_{11}	5.0
$U0.97Th_{0.03}Be_{13}$	0.4
Superconductive	
$PuCoGa_5$	18.0
URu_2Si_2	1.5
UBe_{13}	0.9
$U_{0.97}Th_{0.03}Be_{13}$	0.6
$CeCu_2Si_2$	0.65
UPt_3	0.5
No Ordering	
$UAuPt_4$	0.15*
$CeAl_3$	0.02*
$CeCu_6$	0.02*
UAl_2	0.02*
LiV_2O_4	0.02*

* Lowest temperature measured

Table 1.1. Ordering temperature of various heavy fermion materials with different ground state configurations. Data taken from [1, 15, 16].

The variations in the magnetic ground states in these materials is a result of the competition between the RKKY interaction and the Kondo effect. Since they both depend on the same exchange interaction, J, between the *f*-electron moments and the conduction electrons, materials with different values of J may have different magnetic ground states. For example, in intermetallic Uranium compounds, the exchange parameter J depends in part on the inter-Uranium distance, $d_{U\text{-}U}$. For $d_{U\text{-}U} > 3.6$Å the compounds are generally magnetic at low temperature, while for $d_{U\text{-}U} < 3.4$Å the compounds generally have a non-magnetic ground state [17].

In the case of URhGe and UCoGe, the ground state is a ferromagnetic, and is also related to the inter-Uranium distance, which governs the strength of the interaction. This will be discussed in more detail in the later sections on the particular materials.

1.2 Heavy Fermion Superconductivity

The first heavy fermion system that was found to be superconducting was $CeCu_2Si_2$ [18,19]. Superconductivity was unexpected, since this system has superconductivity coexisting with the strong, localized Ce moments. In the conventional Bardeen-Cooper-Schrieffer (BCS) theory of superconductivity, magnetism and superconductivity cannot cooperatively co-exist, since it makes spin singlet pairing unlikely [20]. The coexistence of magnetism and superconductivity might lead to competition in real space between magnetic and superconducting volume fractions [21].

Heavy fermion superconductors are known to be type-II superconductors [12], and most have transition temperatures $T_C \leq 2K$, though T_C's as high as 18K have been reported [22]. Properties of some heavy fermion superconductors are summarized in Table 1.2.

Material	T_c (K)	λ (1000 A)	ξ (A)	H_{c1} (0) (mT)	H_{c2} (0) (T)
$PuCoGa_5$	18.5	1.24	21	35.0	74
$CeCu_2Si_2$	0.7	>4	90	2.3	2.0/2.4
URu_2Si_2	1.2	>15/9-10	100-150	1.4	14/3
UPd_2Al_2	2.0	5/5	85	1.0	3.0/3.6
UNi_2Al_2	1.0	>3	240	1.5	1.5
UPt_3	0.55	6-7/6-7	100-120	3.0	2.8/2.1
UBe_{13}	0.9	>8	100	4.6	10.1

Table 1.2. Selected properties of some known heavy fermion superconductors at ambient pressure. Values indicated by slashes (\) refer to different crystallographic directions. Dashes (-) indicate a range of measured values. Data taken from [12, 22].

It can be seen that in addition to the low transition temperatures, these heavy fermion superconductors have large magnetic penetration depths, and small coherence lengths. This is expected, given the large effective mass of the electrons, since

$$\lambda \propto (m_{eff} / n_s)^{1/2} \tag{1.1}$$

$$\xi \propto n^{1/3} / (m_{eff} * T_C) \tag{1.2}$$

where λ is the magnetic penetration depth, ξ is the coherence length, n_s is the superconducting pair density, n is the conduction electron density, and m_{eff} is the effective electron mass.

This leads to very small values of H_{c1} and very large values of H_{c2} by the relations

$$H_{c1} \propto 1/\lambda^2 \tag{1.3}$$

$$H_{c2} \propto 1/\xi^2 \tag{1.4}$$

which means that the heavy fermion superconductors can be studied in the vortex state over a large field range, though the large penetration depth is harder to measure.

Despite this unconventionality, the heavy fermion superconductors display a large jump in the specific

heat at T_C, which indicates a pair coupling strength that is in line with BCS predictions [12]. Since this jump is on the order of $C_p \sim \gamma T_C$, this 2nd order phase transition must be due to the condensation of heavy electrons.

The first experimental proof of an unconventional gap structure in the heavy fermion systems came from measurements of the specific heat, sound attenuation and NMR spin-lattice-relaxation rate in $CePd_3$ and $CeCu_2Si_2$ below T_C [18,19]. These measurements were of a power-law form, not exponential as would be expected for a nodeless gap. This is indicative of an anisotropic gap, but does not uniquely determine the gap structure.

Further evidence for unconventionality in the gap structure of heavy fermion materials came from studying heavy fermion materials with dilute substitutional impurities. In conventional *s*-wave superconductor, magnetic impurities cause exchange scattering that destroys Cooper pairs, and inhibits superconductivity [23]. By contrast, an *s*-wave superconductor should be virtually unaffected by the substitution of non-magnetic impurities. This was found not to be the case for heavy fermion superconductors, where non-magnetic impurities were as effective in destroying superconductivity as magnetic impurities [24].

The decisive evidence for an unconventional gap structure came from specific heat measurements of UPt_3, which showed two superconducting transitions in zero applied field [25]. Measurements in field revealed a complex phase diagram with at least three distinct superconducting phases [26, 27]. Other measurements in applied pressure and applied field have shown magnetic correlations [28] and magnetic penetration depth anisotropies [29]. These measurements have been taken as evidence of line nodes in this material [30].

Some, but not all, heavy fermion systems display these types of features. This indicates, in most cases, the presence of gap nodes in non-*s*-wave superconductors. There is still some debate on the exact nature of

the gap symmetry in some of these materials. All of this is clear evidence that the heavy fermion materials display unconventional superconductivity.

Material	Effective Moment (μ_B)
UPt_3	0.02 [1]
URu_2Si_2	0.02 [1]
UNi_2Al_3	0.2 [1]
UPd_2Al_3	0.85 [1]
$CeCu_{5.9}Au_{0.1}$	1.5 [2]

[1] From: A. Amato. *Rev. Mod. Phys.* **69** (1997) 1119

[2] From: A. Schroeder *et al. Nature.* **407** (2000) 351

Table 1.3. Effective moment sizes of various heavy fermion materials at low temperature.

With the existence of both magnetism and superconductivity in this family of materials, there is the opportunity to study superconductivity and magnetism in close proximity, and in some cases, in coexistence. It is also interesting because the range of effective moment size can vary over a large range within the family of heavy fermion materials. Table 1.3 shows the moments sizes for some heavy fermion materials. This coexistence and variation allows an analysis of the interplay between these effects, and is the focus of this thesis.

1.3 Ferromagnetism and Superconductivity

Heavy fermion materials display a wide variety of magnetic states, as seen above. However, these materials were not the first materials to demonstrate the coexistence of magnetism and superconductivity. Here, the focus is on the coexistence of ferromagnetism and superconductivity.

Two families of ferromagnetic superconductors were discovered before the heavy fermion superconductors, the moly-sulphides such as $HoMo_6S_8$ and the rare-earth sodium borides such as $ErRh_4B_4$ [31]. However, in these materials, the magnetism is due to the rare-earth moments, but the superconducting conduction electron bands are separate and interact weakly with the moments [12].

In the heavy fermion ferromagnetic superconductors, the moments interact strongly with the superconducting conduction electrons via the Kondo effect. Thus, the discovery of the first heavy fermion ferromagnetic superconductor, UGe_2, generated much interest in the possibility of magnetically-mediated pairing, through the formation of triplets [31, 32]. UGe_2 has a moment size of approximately $1.4\mu_B$ at ambient pressure [32], reducing to $0.8\mu_B$ near its quantum critical point of 15kbar [33, 34, 35]. Superconductivity emerges at a pressure of 9kbar, with a peak around 12kbar, where $T_{SC} = 0.8K$ [32].

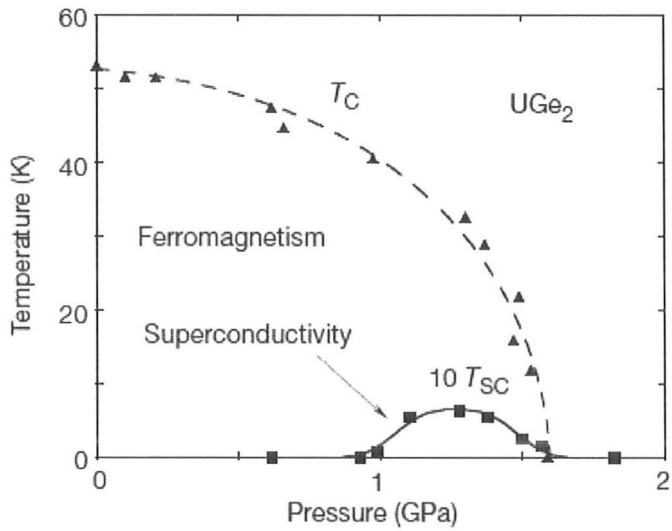

Figure 1.1. The temperature-pressure phase diagram of UGe_2. The superconducting transition, T_{SC}, is taken from a 50% drop in resistivity. Lines are only a guide to the eye. Figure taken from [32].

At the quantum critical point, ferromagnetism and superconductivity disappear simultaneously. This indicates that they may be related phenomena, not competitive as other ferromagnetic superconductors. This relationship would be a good candidate for magnetically-mediated superconductivity, and thus UGe_2 became

the focus of much research.

Using various local probes such as μSR, it has been shown that magnetism and superconductivity can coexist on a microscopic scale for the heavy fermion superconductors [36, 37]. This is in contrast to some other magnetic materials where magnetism and superconductivity exist in phase-separated regions. This is further evidence of strong coupling between magnetic moments and superconducting conduction electrons.

1.4 URhGe

Soon after the discovery of UGe_2, the material URhGe was discovered [38, 39]. It has the orthorhombic TiNiSi structure (space group *Pnma*), shown in Figure 1.2. The lattice constants are given in Table 1.4. This structure differs from the orthogonal structure of UGe_2 (space group *Cmmm*), where the lattice constants are a=4.0089Å, b=15.0889Å and c=4.095Å [40]. These differences are due to the replacement of one Ge site in UGe_2 with a Rh atom.

Although they have different crystal structures, the magnetic structure is very similar. Both materials contain zig-zag chains of nearest-neighbour U-atoms [35]. This feature is important for magnetism, and possibly for superconductivity. The other significant difference is that the magnetic moment of UGe_2 is aligned along the a axis (along the U-U chains) whereas the moments align along the c axis in URhGe (perpendicular to the U-U chains) [35].

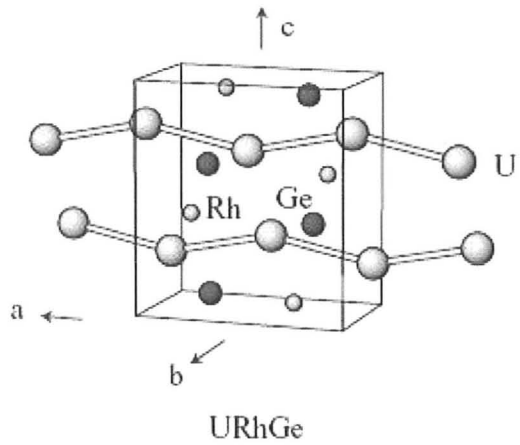

Figure 1.2. The orthorhombic TiNiSi structure of URhGe. This structure is present at all temperatures. Figure taken from [35].

Direction	Spacing (Å)
a	6.87
b	4.33
c	7.51

Table 1.4. The lattice constants of URhGe at ambient pressure. Data taken from [38].

URhGe is a ferromagnet, with T_{Curie}=9.5K, and a superconductor, with a maximum T_{sc}=300mK. These values, particularly the superconducting transition temperature, are strongly sample-dependent. This material behaves, at ambient pressure, much like UGe_2 near its quantum critical point. This is reflected in the U-U distance, 3.5Å in UGe_2 versus 3.48Å in URhGe, as well as the moment size, $0.8\mu_B$ versus $0.42\mu_B$, ferromagnetic transition, 15K versus 9.5K, and superconducting transition, 0.23K versus 0.25K [41]. See Table 1.5, below.

	URhGe	UGe2 (15kbar)
T_{curie} (K)	9.5	15
T_{sc} (K)	0.25	≈ 0.23
μ_s (μ_B)	≈ 0.42	0.8
d_{U-U} (A)	≈ 3.48	≈ 3.5
$\gamma = C/T$ (mJ mol^{-1} K^{-2})	160	120

Table 1.5. Comparison of selected properties of URhGe and UGe_2. These properties suggest that URhGe should be in close proximity to a quantum critical point. Data taken from [41].

Since the quantum critical point of UGe_2 is 16kbar, based on the data in Table 1.5, one would expect URhGe to also be near a critical point. This has been the focus of study, and the temperature-pressure phase diagram of URhGe is given in Figure 1.3.

In contrast to the case of UGe_2, there is no common critical pressure for ferromagnetism and superconductivity. More surprisingly, the Curie temperature increases with applied pressure. This may suggest that the nature of the critical point is different between UGe_2 and URhGe, and there are more parameters that need to be considered than those listed in Table 1.5.

Another aspect of the URhGe phase diagram that was recently discovered is reentrant superconductivity with large applied field. This is shown in the Temperature-Field phase diagram shown in Figure 1.4.

This effect is not unique to URhGe, but it is unusual that this field induced superconductivity occurs for a range of angles of the applied field, from 30° to 55° [39], and is very anisotropic [43]. This implies that this effect is not caused by a cancellation due to the magnetic moments. The maximum T_{SC} occurs at a field H_R above which the magnetization collapses abruptly to zero. Such fields exist in other materials, but the peak of superconductivity at this field is unique to URhGe [39, 44]. This region of field induced superconductivity has been speculated to be due to ferromagnetic spin fluctuations, but there is no generally-

accepted explanation for this phenomenon [39, 42].

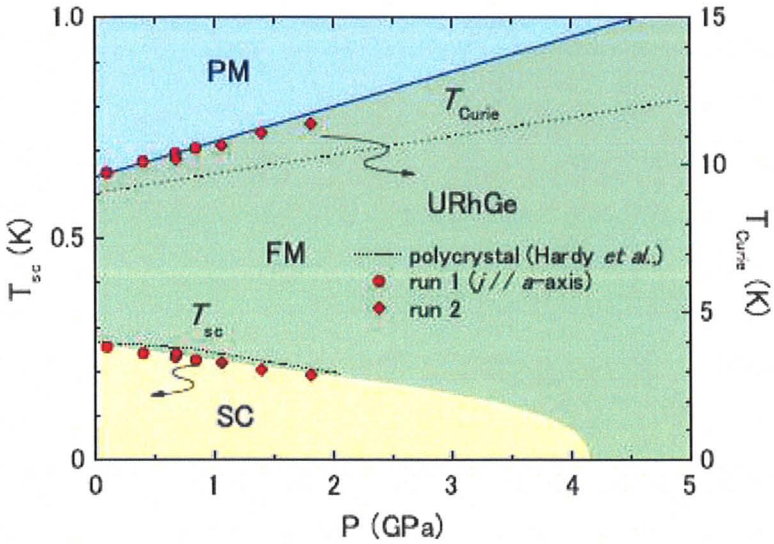

Figure 1.3. Pressure-temperature phase diagram of URhGe. This shows an increase in T_{Curie} with applied pressure, and a critical pressure for superconductivity at 4.1GPa. Figure taken from [42].

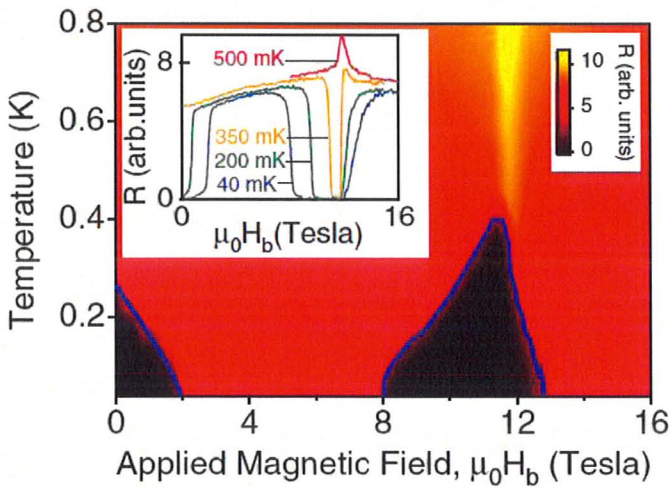

Figure 1.4. Magnetic field-temperature phase diagram of URhGe. The field was applied along the *b* axis. This shows a critical field around 2T, and reentrant superconductivity between 8 and 12.5T. Figure taken from [39].

Though much work has been done on this compound, it can be seen that there is a significant gap in the understanding of the magnetic correlations, and the effect of magnetic moments on superconductivity.

1.5 UCoGe

A similar material, UCoGe, was also discovered [45], with the same structure as URhGe, orthorhombic TiNiSi (space group *Pnma*) with slightly different lattice constants. The lattice constants of UCoGe are approximately 3% smaller than those of URhGe due to the smaller atomic radius of Co compared to Rh. The lattice parameters of UCoGe are summarized in Table 1.6. It can be seen that these lattice constants are very close to those of URhGe, so we should expect similar properties.

UCoGe behaves similarly to URhGe, as UCoGe is also a ferromagnet (T_{curie}=2.8K) and a superconductor (T_{sc}=800mK) at ambient pressure. The phase diagram of UCoGe is shown in Figure 1.5.

Direction	Spacing (Å)
a	6.845
b	4.206
c	7.222

Table 1.6. The lattice constants of UCoGe at ambient pressure. Data taken from [45].

There are several obvious differences to the phase diagram of URhGe. Most noticeably, the Curie temperature decreases with applied pressure. There is also no signature of a ferromagnetic transition above P ≈ 1GPa, down to 400mK [46]. Superconductivity also appears surprisingly stable against hydrostatic pressure, persisting above 2.4GPa. This means that unlike UGe_2 and URhGe, superconductivity exists in the paramagnetic state in UCoGe.

A possible explanation of this has been suggested from NMR/NQR measurements on UCoGe. They find that the superconducting volume fraction is approximately 30%, and that the superconducting fraction

exists both in regions of ferromagnetism, and paramagnetic regions of the sample [47]. This is in contrast to NMR/NQR measurements on UGe_2, which find that the superconducting volume fraction exists only in ferromagnetic regions of the sample [34]. The reason for the difference between the superconducting fraction in these two materials remains an open question at this time.

One of the interesting features of UCoGe is its extremely small ordered moment ($m=0.03\mu_B$) [45]. This is not unusual for the heavy fermion materials, but it is much smaller than the other ferromagnetic superconductors. The hope is that the small ordered moment will allow for the study of the superconducting mechanism with only a small ferromagnetic component. Comparison with URhGe and UGe_2 may be able to highlight the effect of a different magnetic moment size on superconductivity, particularly in the context of magnetic spin fluctuations mediating the Cooper pairing in these materials.

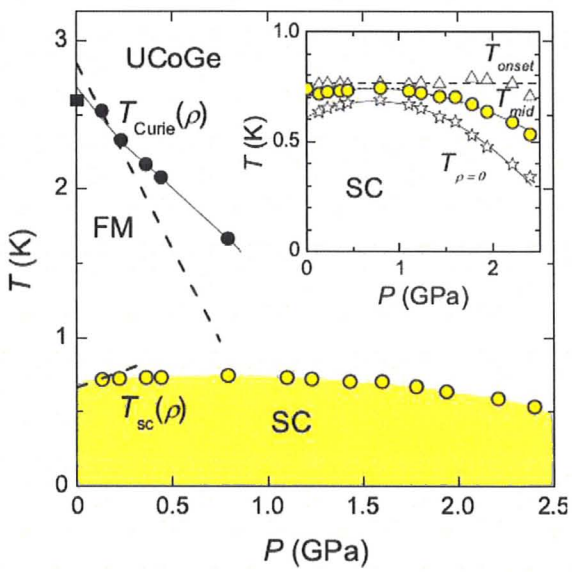

Figure 1.5. Pressure-temperature phase diagram of UCoGe. This shows an decrease in T_{Curie} with applied pressure. Figure taken from [46].

Recent measurements of H_{c2} in UCoGe show anisotropy, with a smaller critical field in the direction of the magnetic moments [48]. This work agrees with theoretical calculations [49], which is taken as evidence of point nodes along the *c*-axis (parallel to the magnetic moments), and possibly the existence of multiple

superconducting bands. This is something that has yet to be experimentally proven. A sensitive magnetic probe such as μSR would be a good candidate for investigating multiband superconductivity by measuring the penetration depth, and the possibility of magnetic fluctuations in this material.

Future work on this system involves looking for the features mentioned previously, as well as to explore the nature of the phase separation between the paramagnetic and ferromagnetic regions. Finally, comparing these results to URhGe would provide clues as to the influence of magnetic moments on the pairing mechanism in these materials. Since the two materials have nearly the same physical properties, the differences in the ferromagnetic properties may directly give rise to the differences in superconducting properties of these samples.

II. Experimental Methods

2.1 Crystal Growth

All of the samples were grown at the Brockhouse Institute for Materials Research at McMaster University. The samples were also given additional heat treatment, as described below. The samples were prepared from high purity (99.9% Uranium) depleted Uranium (≥ 99.5% U-238). The other constituents were also used in high-purity forms: Rh (99.99%), Co (99.99%), and Ge (99.999%). For each growth, the constituents were arc-melted in a mono-arc furnace (see Figure 2.1), in stoichiometric amounts, 1:1:1 U:Rh/Co:Ge. The resulting boule was cooled, flipped, and remelted at least once to ensure uniformity.

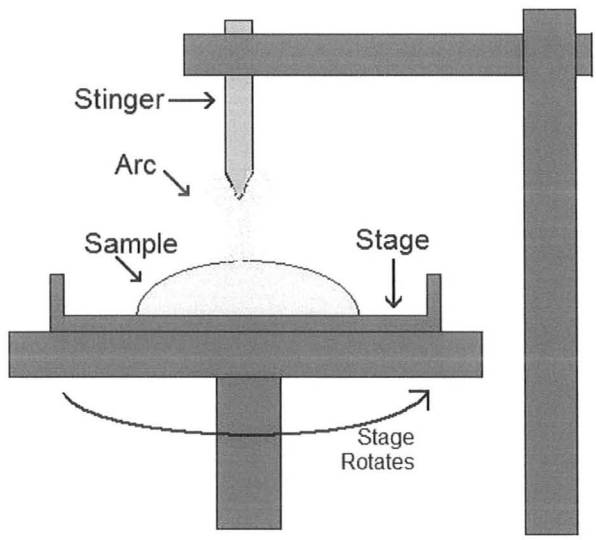

Figure 2.1. Schematic of a mono-arc furnace. The sample is placed on the stage, and a high voltage supply creates an arc from the stinger to the sample, heating the sample. The stage is rotated to heat the sample uniformly, and facilitate mixing. The entire setup is enclosed in a glass bulb, back-filled with Ar gas.

The boule was then placed into a tri-arc furnace (see Figure 2.2) and the crystals were grown by

Czochralski pull under a continuous gettered Ar atmosphere. This method is commonly used to grow large single crystals of materials such as Si and GaAs, and is described in detail elsewhere [50].

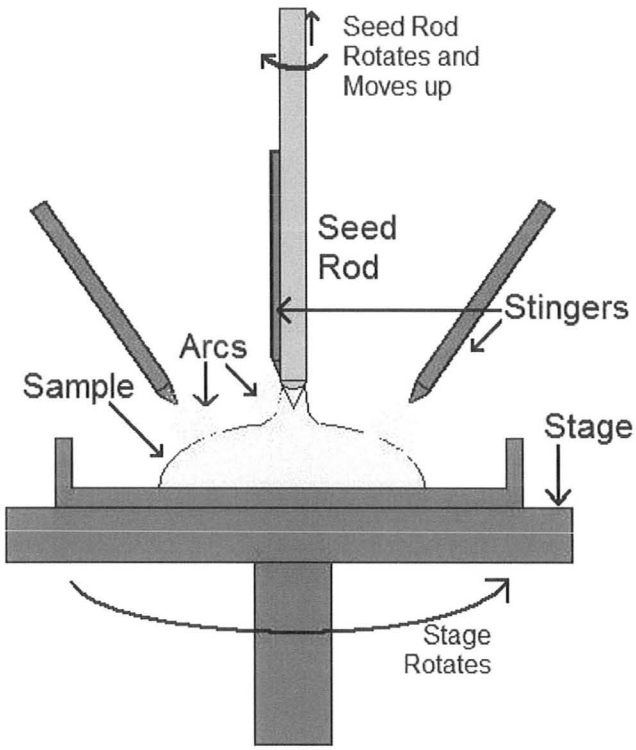

Figure 2.2. Schematic of a tri-arc furnace. The sample is placed on the stage, and a high voltage supply creates an arc from the three stingers to the sample, heating the sample. A seed rod is lowered into contact with the molten sample, then pulled upwards. The seed rod is cooled with water, so that the sample crystallizes on the seed rod, with the molten sample below. The seed rod and stage are counter-rotated to create a straight crystal. The entire setup is enclosed in a glass chamber, back-filled with Ar gas.

The Czochralski method involves melting the material to be grown in a crucible, and lowering a seed rod into the melt. The seed rod is kept below the melting point of the material, so that material solidifies onto it. The seed rod is pulled upwards, at varying speed depending on the growth, to gradually solidify more material. The rod is rotated while moving upwards to promote homogeneity and remove defects.

The as-grown crystals were approximately 30-40mm in length, with varying diameters, ranging between 1 and 10mm. The most uniform, and most likely part of the sample to be single-crystal, is the later part of growth (end of the crystal). However, the Czochralski method tends to accumulate impurities near

the end of the growth [50], so care must be taken to ensure that any possible impurities are removed before the growth.

After the first growth of each sample, the as-grown samples were then wrapped in Ta foil, sealed in quartz tubes under high vacuum, and annealed for 5 days at 900°C, following the procedure given in [46, 51]. Crystals grown in the second growth were annealed for 14 days at 900°C, following a modified procedure of [52]. In total, two growths of UCoGe and two growths of URhGe were performed.

To analyze the quality of the growths, resistivity measurements were done, and the residual resistivity ratio (*RRR*) was calculated by

$$RRR = \rho(300\text{K}) / \rho(1\text{K}) \qquad (2.1)$$

A larger value of *RRR* generally indicates a better quality sample, as the resistivity at low temperature is affected largely by the effects of impurity scattering. The absolute value depends on the material being studied. Other studies have reported *RRR* = 10 [45], 20 [53], 25 [45], 28 [46] and 30 [48, 54] for UCoGe, and *RRR* = 7 [38], 12 [44], 16 [44], 21 [52], 40 [44] and 50 [39, 42] for URhGe. This range of values indicate that sample quality can vary greatly, and that the optimal growth conditions and annealing procedure is not yet refined. Despite this, measurements comparing samples of different qualities show some similarities and consistencies. Some lower-quality samples have been shown not to become superconducting, highlighting that there is still a need to consider sample quality in the measurements.

The procedure used in preparing the samples generated residual resistivities comparable to those reported elsewhere. For the first set of crystals, the value obtained was *RRR* = 3.5 for UCoGe, and was not calculated for URhGe, since it was produced at the same time as the better-quality second batch.. The second batch of samples was found to have *RRR* = 2.5 for UCoGe and *RRR* = 10 for URhGe. The results of measuring the residual resistivity will be further explained in sections 4.2 and 5.2 concerning the DC Resistivity measurements.

2.2 Structure Characterization Techniques

To analyze the structure and further examine the crystal quality, three types of measurements were performed: Laue X-ray diffraction, powder X-ray diffraction and Scanning Electron Microscopy. These techniques are explained below.

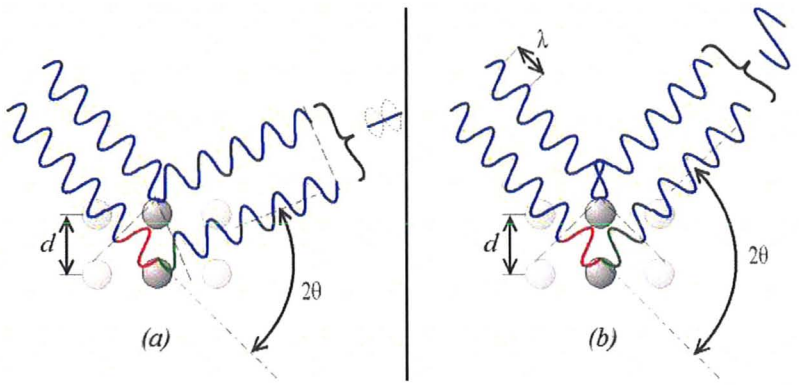

Figure 2.3. X-ray scattering in a crystal. *(a)* Destructive interference. The photons are out of phase, and they cancel. *(b)* Constructive interference. The scattered photons are in phase, and they interfere constructively.

X-ray diffraction is based on Bragg scattering of (X-ray) photons. When a photon is incident on a crystal, there will be scattering in all directions. In a random direction, the scattered photons will be out of phase with each other, having scattered off different atoms (see Figure 2.3a). At these angles, the photons cancel one another, and on average, no scattered photon intensity can be measured. However, at certain angles in a crystallographic plane, photons scattered from adjacent atoms are in phase, and a peak in the scattering intensity is observed (see Figure 2.3b), since there is no cancellation. This corresponds to angles where the difference in length to the detector is an integer multiple of the photon wavelength. This condition is known as Bragg's Law, and is given by,

$$n\lambda = 2d\sin\theta \qquad (2.2)$$

where n is an integer, λ is the wavelength of the scattered photons, d is the inter-atomic spacing, and 2θ is the angle between the incident and scattered photons. This corresponds to the variables in Figure 2.3. The value of d depends on the angle of the crystal relative to the scattering plane. For Laue diffraction, scattering can occur in any angle θ, as well as any angle φ, which is the angle in the plane perpendicular to the incident photons. Consequently, a Laue pattern will show the φ-dependence of the scattering.

These Bragg peaks can be observed from all possible pairs of crystallographic planes. However, as the distance between planes increases, the angle of diffraction approaches 180°, and the signal becomes lost in the background. Therefore, the most reliable reflections to use for indexing the crystal structure are the lower indices, which will be the reflections that are most easily observed.

Laue X-ray diffraction produces a diffraction pattern similar to that shown in Figure 2.4. This image is a representation of the reciprocal lattice of the crystal structure. This can be used to analyze the crystal structure, since multiple grains would produce multiple patterns that can be misaligned. However, the typical X-ray penetration depth is on the order of 1μm [55], so Laue diffraction will only probe the local surface quality. This is often observed when different areas of the surface will exhibit different quality when imaged with Laue diffraction.

The main use of Laue diffraction is for aligning crystals. Since the reciprocal lattice pattern has the same symmetries as the real space lattice, we can identify points in the Laue pattern based on the symmetries. For example, if a crystal being measured has a tetragonal structure, and a two-fold symmetric point is observed in the Laue pattern, it must be the c-axis. By fitting the symmetries and the spacing between peaks, the orientation of the crystal can be determined.

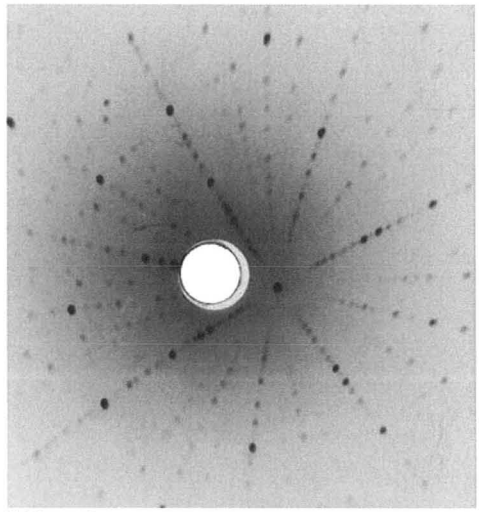

Figure 2.4. Example of a Laue diffraction pattern. This pattern was obtained from a single crystal of La_2CuO_4. The high-symmetry point near the centre is one of the major axes.

Powder X-ray diffraction uses a similar principle. If the sample is ground into a powder, then the alignment information is lost. The Bragg peaks can still be found at various θ angles, but the measurement is essentially integrating over all possible φ values. As the detector is moved through the possible θ values, peaks corresponding to the various indices will be observed. These angles again follow Equation (2.2) above, but now d is the distance between any pair of lattice points. In theory, the measurement of intensity versus θ would display a series of delta functions at the angles corresponding to the Bragg peaks, with the intensity determined by the number of pairs that allow that scattering angle. However, in reality, these peaks have some width due to thermal motion of the atoms, as well as crystal defects. An example of this pattern is shown in Figure 2.5.

The advantage to performing powder X-ray diffraction is to measure the structure and lattice constants. Since all reflections can be seen, one does not need to assume a particular crystal structure to analyze the data. Instead, the pattern can be used to calculate the crystal structure and the lattice constants of the system based on the constituent atoms.

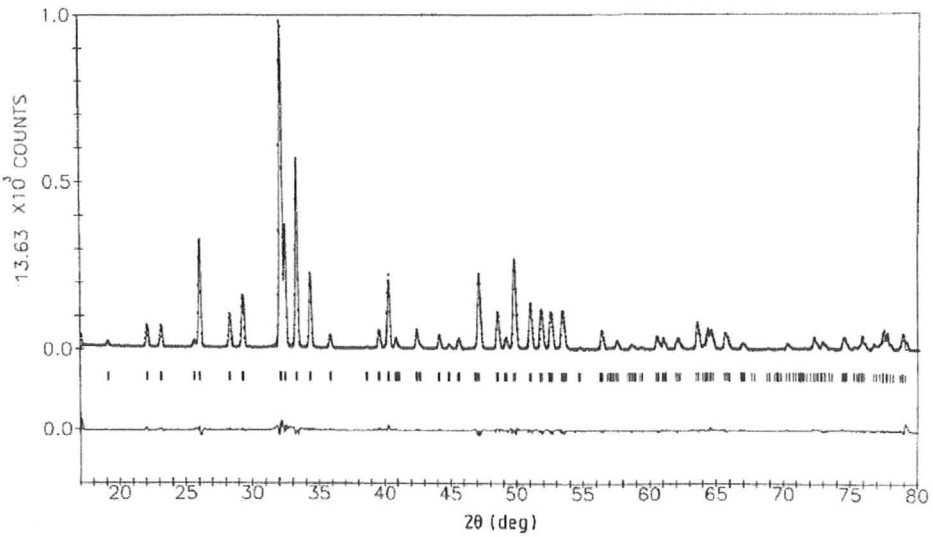

Figure 2.5. Example of a powder X-ray diffraction pattern. The upper set of peaks is the measured data. The vertical lines below that indicate the positions of the Bragg peaks. The line at the bottom is the difference between the measured and calculated values, based on the calculated structure. Figure taken from [56].

The third method that was used to characterize the structure was electron microscopy. The measurements performed in this study were on done on a piece of URhGe, using a scanning electron microscope (SEM). Electron microscopes operate by using electron beams, typically on the order of 100-400keV, to probe the near-surface of materials. Scanning electron microscopes are used for bulk samples, like the crystal measured here, since electrons cannot penetrate samples thicker than a few hundred nanometres. Scanning electron microscopy uses various detection methods, utilizing back-scattered electrons, secondary electrons, or x-rays. These often have similar imaging properties, though there are slight differences in magnification resolution and depth resolution.

The advantage to using electron microscopy is that it can provide very detailed images of small parts of the sample. In the case of samples like the ones presented here, this can be used to study physical properties, including crystal quality, growth properties, and surface properties. The specific applications to this study will be discussed in more details in Section 5.1.

2.3 DC Resistivity

Resistivity measurements on small samples, at very low temperatures are complicated by the fact that the resistance of the sample becomes very small. Because of this, a traditional two-point resistance measurement will not work, as the ohmmeter leads will have a non-negligible resistance. For this reason, a four-point resistance measurement was used. This measurement uses four leads attached to the sample, two on each end. On each end, there is a lead for injecting current, and a lead for measuring voltage. The schematic is shown in Figure 2.6.

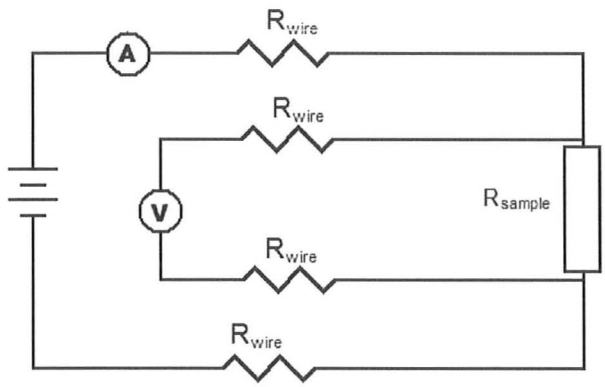

Figure 2.6. Schematic representation of a four-wire resistance measurement. This method isolates the resistance of the sample from that of the components.

Because the sample resistance is very small, the resistance of the leads becomes comparable to, if not greater than, that of the sample. A simple two-point measurement would not be able to distinguish the resistance of the sample from that of the leads. With the four-point measurement, two leads are set up to form a series circuit with an ammeter. The other two leads set up a voltmeter in parallel to the sample. Since the internal resistance of a voltmeter is high, it draws negligible current. Therefore, nearly all of the current measured by the ammeter passes through the sample. Since there is almost no current travelling through the potential leads to the voltmeter, the voltage recorded by the voltmeter is almost exclusively

caused by the sample. Since we now have the current and the voltage across the sample, the resistance of the sample is calculated by,

$$R = V / I \tag{2.3}$$

where V is the voltage measured by the voltmeter, and I is the current measured by the ammeter.

All of our resistance measurements were done with this method.

2.4 Bulk Magnetometry

Bulk magnetometry measurements were performed using a Quantum Design SQUID Magnetometer. The schematic of this system is given in Figure 2.7. The SQUID magnetometer is designed to measure the magnetization, **M**, of the sample in response to an applied magnetic field, **H**. This can be studied as a function of temperature and applied field to gain information about the properties of various condensed matter systems [57, 58]. Sharp changes in the magnetization can be used to identify phase transitions in the material.

The most general form of magnetization as a function of temperature and field is usually expressed as a Taylor series. Since magnetization is an odd function of the field, only the odd powers need to be considered in the expansion, leading to the expression,

$$M(T,H) = \sum_{1}^{\infty} \frac{\chi_{2n-1}(T)}{(2n-1)!} \cdot H^{n} \tag{2.4}$$

$$M(T,H) = \chi_{1}(T) \cdot H + \frac{\chi_{3}(T)}{3!} \cdot H^{3} + \ldots \tag{2.5}$$

where $M(T,H)$ is the magnetization, H is the applied field, and χ_n, the n-th order magnetic susceptibility, is

the n-th derivative of **M** with respect to **H**. Equations (2.4) and (2.5) assume **M** || **H**.

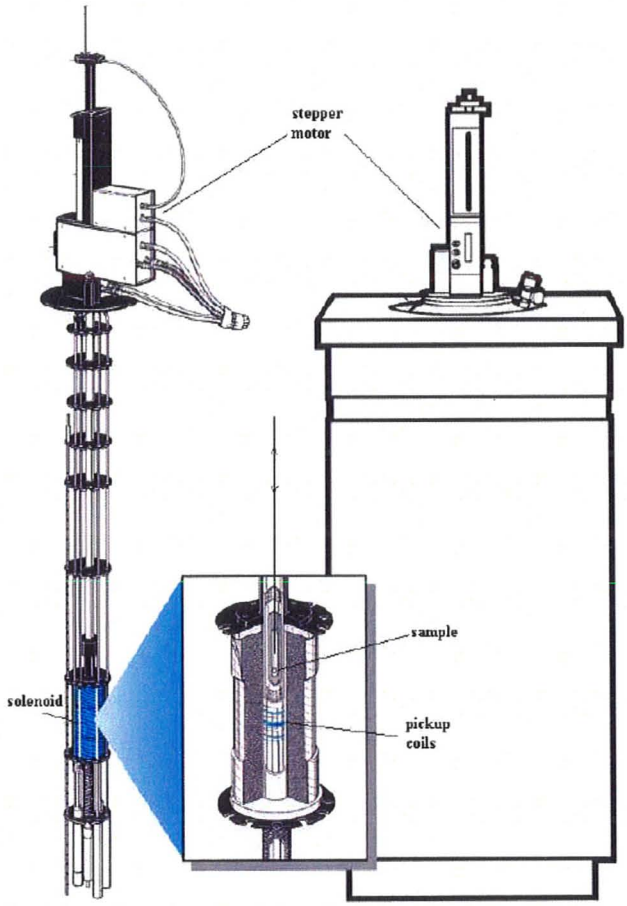

Figure 2.7. Schematic representation of the SQUID magnetometer. The inset shows the sample space and the four pickup coils. Figure taken from [59].

In low fields, the terms that are cubic and higher in the magnetic field can often be neglected. Thus, the linear susceptibility, χ_1 , becomes the dominant term. This can take on many different forms, but for many magnetic systems such as ferromagnets above their Curie temperature, the linear susceptibility is well-approximated by the Curie-Weiss law,

$$\chi_1(T)=\frac{C}{T-\theta} \qquad (2.6)$$

where C is the Curie constant and θ is the Weiss constant. In general, C is proportional to the square of the magnetic moment, and θ is positive for a ferromagnet.

A **S**tandard **QU**antum **I**nterference **D**evice (SQUID) functions by using a loop of a superconducting material, which is broken by one or two Josephson junction(s). When this loop is coupled to an LC circuit, a voltage can be measured that depends on the amount of magnetic flux enclosed by the superconducting loop [60]. This can measure extremely small changes in magnetic flux. In theory, a SQUID of this design could measure magnetic fields as small as 10^{-19} T.

The SQUID used here is an rf-SQUID, which uses only one Josephson junction, and is based on the ac-Josephson effect. This occurs when the magnetization of the sample induces a current in the superconductors of the Josephson junction, creating a voltage difference across the junctions. This voltage difference is used to drive another "tank" circuit. The resonant frequency in the tank circuit is quantized due to the properties of the Josephson circuit, and so is a periodic function of the magnetic flux [61, 62]. By measuring the tank circuit, the magnetization of the sample can be calculated.

The SQUID used for the measurements presented here actually contains four pickup coils connected in series instead of one (See Figure 2.7). Two of the coils are placed in the centre of the sample space, and the other two are positioned above and below the sample, wound in the opposite direction. As a result of the signals between the coils, the SQUID is not sensitive to background fields that are constant, or linear in space. The sample is gradually moved vertically in the sample space, and a voltage versus position graph is obtained. This allows the sample to be centred in the coils to correctly reduce the background signal.

The SQUID is cooled with liquid He-4, giving an operating temperature range of 1.7K to 300K. It also contains a superconducting solenoid, allowing measurements in fields up to 5.5T.

III. Muon Spin Relaxation/Rotation (*μSR)*

3.1 Principles of μSR

The technique of μSR is an experimental technique for measuring the local magnetic properties of condensed matter systems. The acronym stands for various terms, depending on context, including muon Spin Relaxation, Rotation, Resonance and Research. This is intended to highlight the features of μSR, as well as to draw parallels with other condensed matter techniques, such as NMR (nuclear magnetic resonance) and ESR (electron spin resonance). Like these techniques, μSR is a real-space probe of the magnetic moments in the system. Unlike them, however, μSR uses polarized particles from outside the system, rather than polarizing the nuclear or electronic spins already present. Thus, μSR does not need to measure the response of the system to the probe, but rather the response of the probe to the system.

Muons are leptons, like electrons, and share many of the same properties. They have spin ½, and a charge $\pm e$. However, they are more massive, with a rest mass of $m_\mu = 207m_e$, and a gyromagnetic ratio of $\gamma_\mu = 2\pi \times 135.54 \frac{MHz}{T}$. The muons used for μSR experiments are generated in particle accelerators, from the decay of pions. This involves accelerating protons, and colliding them with low-Z targets. In the case of the experiments in this thesis, the target was a material such as Beryllium or Carbon. At TRIUMF, where the measurements were performed, the incident protons have energies of ~500MeV. Three principle processes involved in these collisions are responsible for pion generation [63],

$$p + p \rightarrow p + n + \pi^{+} \tag{3.1}$$

$$p + n \rightarrow n + n + \pi^{+} \tag{3.2}$$

$$p + n \rightarrow p + p + \pi^{-} \tag{3.3}$$

The pions migrate to the surface of the target, and decay by the weak interaction to [63],

$$\pi^{+} \rightarrow \mu^{+} + \nu_{\mu} \tag{3.4}$$

$$\pi^{-} \rightarrow \mu^{-} + \bar{\nu}_{\mu} \tag{3.5}$$

In the rest frame of the pion, weak decay can only produce neutrinos that have spins opposite to the direction of momentum, a feature of parity violation. Since pions have no spin moment, to preserve linear and angular momentum, the muon spin must be aligned opposite to its momentum. So in the type of process described above, using surface pions, an accelerator such as TRIUMF can be used to produce of beam of muons that is nearly 100% spin-polarized.

Using these spin-polarized muons, one can perform μSR experiments. One by one, the muons are implanted into the sample. Using a Wien filter (crossed electric and magnetic fields), the muon spins can be rotated prior to implantation. Since the direction of the electric and magnetic fields are fixed, the muon spin direction can only be rotated in one direction. The Wien filter is also used for removing positrons from the beam, so that only muons are entering the sample space. Upon implantation in the sample, the muons will stop at interstitial sites within the lattice, and will undergo Larmor precession in any local field present at the muon site.

Muons, like electrons, come in two varieties, oppositely charged. Both types can be used for μSR measurements, but negatively charged muons tend to undergo capture by the positively-charged nuclei. This interaction with the system can be used to extract information, but it involves perturbing the system. Negative muons cannot be produced as surface muons, since negative pions tend to be captured in the

sample, so the production method here only works for positive muons. As such, using negatively-charged muons is a more complicated method to study material properties, which is why μSR measurements are nearly always performed with positively-charged antimuons. All of the experiments described in this thesis are done with positively-charged muon beams.

Muons are unstable, decaying with a mean lifetime of $\tau_\mu = 2.127\mu s$. The muons decay through the process [63],

$$\mu^+ \rightarrow e^+ + \nu_e + \overline{\nu}_\mu \qquad (3.6)$$

giving off a positron and two neutrinos. The two neutrinos are not detected in the experiments, but the positron is detected, which is where the information is extracted. The muon decay process is also a weak interaction process that violates parity. Because of this, the positron that is ejected in the decay is emitted preferentially in the direction of the muon spin at the time of decay (see Figure 3.1).

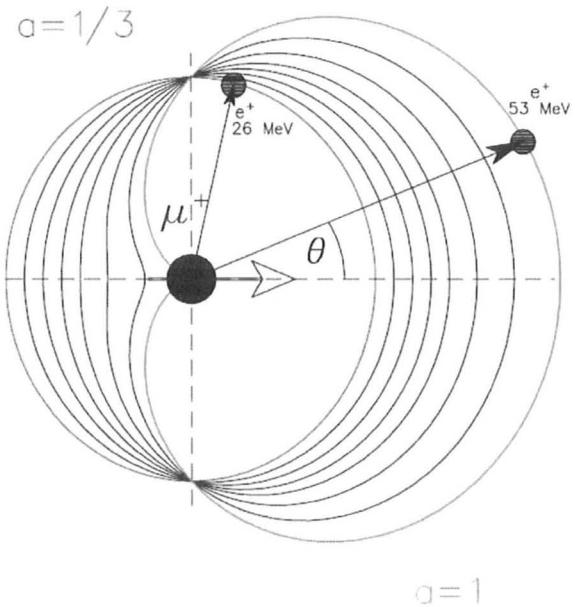

Figure 3.1. Representation of the probability distribution of the positron momentum produced from muon decay (Equation 3.6). This distribution is calculated from the function given in Equation 3.7. Figure taken from [59].

The probability that a positron will be emitted at an angle θ from the muon spin direction is given by [63],

$$W(\theta)=1+a(\epsilon)\cos(\theta) \qquad (3.7)$$

where $a(\epsilon)$ is called the "asymmetry factor", and increases with the kinetic energy of the positron, ϵ. This function is shown for a range of positron energies in Figure 3.1.

The positrons ejected from the sample are detected by counters placed on the six sides of the sample, labelled Up, Down, Left, Right, Forward, and Backward for clarity. These counters are largely insensitive to the energy of the positron, so the asymmetry detected is an integration over all possible positron energies. By detecting many millions of counts, a histogram of counts versus time in each counter can be compiled, and information about the time-dependence of the muon spin in the sample can be extracted. This will be explained in more detail in the following sections.

3.2 Zero-Field (ZF) -μSR

The experimental geometry for a Zero-Field (ZF)-μSR experiment is shown in Figure 3.2. This type of experiment uses muons with their spins aligned antiparallel to the direction of momentum. The muons first pass through a thin scintillation counter, which starts a timer. The muon then enters the sample and its spin precesses around the direction of the local magnetic field, with a frequency,

$$\omega=\gamma_{\mu}H_{loc} \qquad (3.8)$$

If $\hat{z}$ is the initial muon spin direction, then the z-component of the spin evolves in a manner described by [59],

$$S_z(t) = \cos^2\theta + \sin^2\theta \cos(\gamma_\mu H_{loc} t) \qquad (3.9)$$

where $\cos\theta = \dfrac{\mathbf{H}_{loc} \cdot \hat{\mathbf{z}}}{H_{loc}}$.

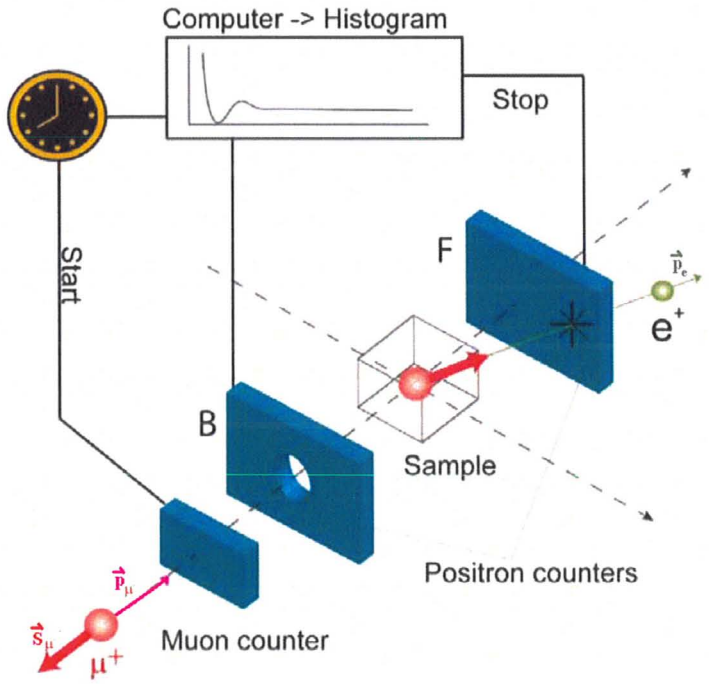

Figure 3.2. The experimental geometry of a ZF- μSR experiment. Here, we define $\hat{z}$ as being the beam direction, $\hat{y}$ is Up-Down, and $\hat{x}$ is Right-Left. Figure taken from [59].

The muon decays at some later time, and emits a positron, which is detected by one of the scintillation counters around the sample. The counters do not cover the entire area, so the event is not always detected. In the case that zero or more than one positron is detected, the event is vetoed. If more than one muon is in the sample space at a given time, this is also vetoed. When the counters detect a good event, it is recorded, stopping the clock. To maximize the good events, and simplify analysis, counters are arranged in pairs on opposite sides of the sample, and one counter is in the direction of the initial muon spin polarization. These are not necessary conditions, but were used in all of the experiments discussed here.

In analyzing the results, the number of counts in a single counter is considered. For the geometry

described in Figure 3.2, where the initial muon spin polarization is in the backwards ($-\hat{z}$) direction, we can express the number of counts in the Forward/Back pair of counters as,

$$N_{B,F}(t) = N_{0B,F}[B_{B,F} + e^{-t/\tau_\mu}(1 \pm A_{B,F} P_z(t))] \qquad (3.10)$$

where the +/- corresponds to Back/Forward, $A_{B,F}$ are the intrinsic detector asymmetries for the Back or Forward counters, $N_{0B,F}$ are normalization factors, and $B_{B,F}$ is a time-independent background signal, which can be measured in the experiment. In general, $A_F \neq A_B$, and we define $A_F = \beta A_B$. However, the factor β is often hard to measure, and except for very thick samples or large differences in the solid angle covered by the counters, $\beta \approx 1$. Finally, $P_z(t)$ is the ensemble average muon spin polarization, along the $\hat{z}$ direction.

The most common way in which to analyze μSR data is to measure the asymmetry function, $A_z(t)$, which is proportional to $P_z(t)$ and is defined as [59],

$$A_z(t) = \frac{(N_{0B}(t) - B_B) - \alpha(N_{0F}(t) - B_F)}{(N_{0B}(t) - B_B) + \alpha(N_{0F}(t) - B_F)} \qquad (3.11)$$

where the parameter α is to account for any possible differences in the counter efficiency, solid angle, etc. This value is not always close to 1, but is easily measured with a μSR experiment in low applied field (~50G).

Since this is proportional to $P_z(t)$, we must consider the way in which this term is calculated. For the case of static magnetic moments within the sample, $P_z(t)$ is obtained by weighting Equation 3.9 with the distribution of magnetic moments at the muon site,

$$P_z(t) = \iiint S_z(t) \mathrm{P}(H_x) \mathrm{P}(H_y) \mathrm{P}(H_z) dH_x dH_y dH_z \qquad (3.12)$$

where $\mathrm{P}(H_z)$ is the probability of the muon seeing a field H_z in the $\hat{z}$-direction, etc.

This local field distribution is what carries the information about the system being studied, and finding the form of $P_z(t)$ is one of the main aims of a μSR experiment. Various functional forms for $P_z(t)$ arise for various cases of the local magnetic moment distribution. These forms can be used to fit to the μSR data,

describing the system in terms of these cases. The forms used for the analysis of μSR data in this experiment will be discussed in Chapters 4 and 5.

3.3 Transverse Field (TF) -μSR

Transverse Field (TF) - μSR experiments involve applying a magnetic field to the sample, in a direction perpendicular to the initial muon spin direction. This can be done either by applying a field perpendicular to the beam direction (with the muon spins antiparallel to their momentum), or by applying a field along the beam direction (direction of the muon momentum) and rotating the muon spins to be perpendicular to their momentum. The latter is the more common method, since large fields tend to deflect the beam when not in the same direction as the muon momentum.

In the presence of this large field, the muon spins will precess at a frequency given by Equation (3.8). These fields are generally much higher than those due to the sample, and so the muons see a field which is very nearly perpendicular to their spin direction. This simplifies the analysis, since we can assume that the field is in the direction of the muon spin, now perpendicular to the beam direction. This simplifies Equation (3.12), since we now have a field that, to a good approximation, is only in one direction. This changes the form of the various functional forms that are used to fit the data. The details of this fitting will be discussed in Sections 4.4 and 5.4.

IV. Measurements of UCoGe

4.1 Structure Characterization

The two samples of UCoGe were grown by the method described in Section 2.1. In order to characterize their structure, both Laue and powder X-ray diffraction measurements were performed.

Samples for powder X-ray diffraction measurements were prepared by grinding a small piece of the polycrystal in a mortar under kerosene to prevent the formation of dust from the material. The ground sample was then placed on a polished Si plate. The Si plate was prepared in such an orientation that it produced no Bragg peaks, and so would not interfere with the peaks from the sample. The plate (and sample) were washed with methanol to remove any residual kerosene.

The sample was measured on a PANalytical X'Pert PRO X-Ray diffractometer at the Brockhouse Institute for Materials Research at McMaster University. The sample is rotated at ~2Hz in the diffraction plane, while the incident X-ray beam and the detector can rotated through a usable 2θ angle of 0° to 160°, due to the placement of the source and the detector. The data was collected by the accompanying X'Pert Data Collector software, Version 2.0.

The powder X-ray pattern of the first crystal is shown in Figure 4.1. There is also a reference pattern for this sample [51], shown in Figure 4.2.

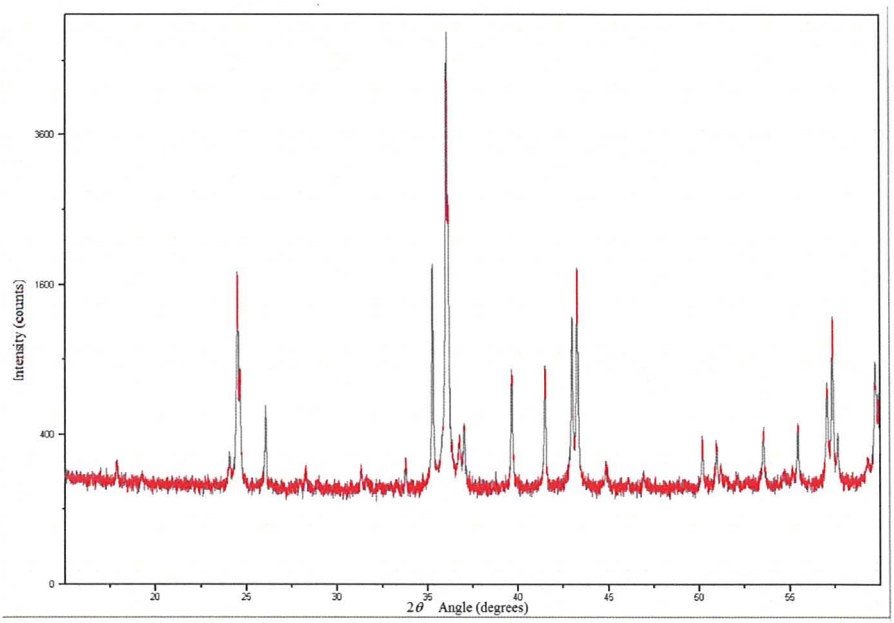

Figure 4.1. The powder X-ray measurements for the first growth of UCoGe. This is plotted as a semi-log plot. Several small impurity peaks are seen, particularly around 37°.

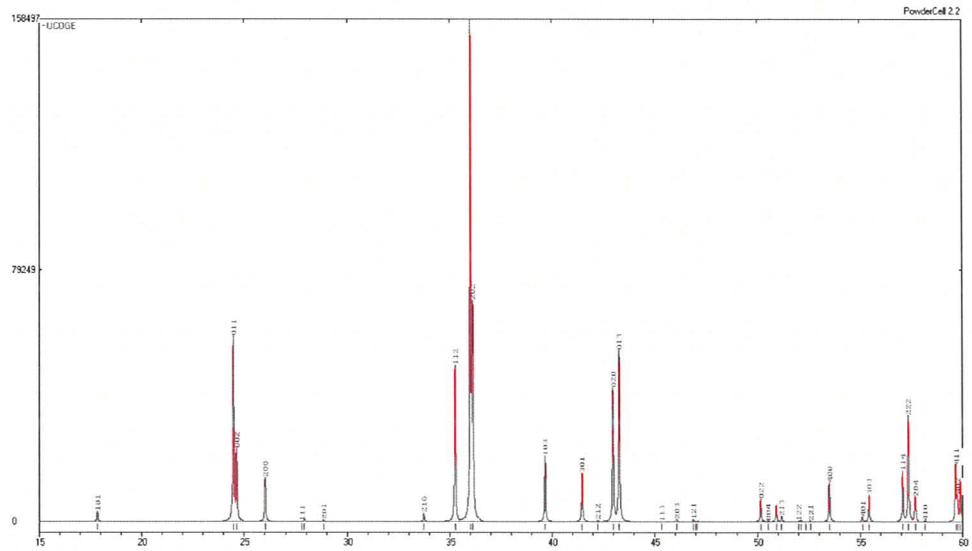

Figure 4.2. The theoretical powder X-ray pattern of UCoGe, based on the data given in [51].

From the similarities in the patterns, we were able to conclude that we had a crystal of UCoGe with the correct phase, the orthorhombic *Pnma* structure. We also concluded that since the measured and calculated patterns were nearly identical, the lattice constants of our sample were very close to those

reported in [51], given in Table 1.6. By performing a rough refinement of the pattern, we determined that our lattice constants were $a = 6.844(3)$, $b = 4.202(2)$ and $c = 7.230(5)$Å .

We also see that there were a few extra peaks, particularly those around $2\theta = 37°$, which can be attributed to impurities in the sample. These peaks have a magnitude that is on the order of 5% the magnitude of the peak at 35.5°, and so the volume of impurities in the sample will be on this order as well. This could produce a measurable impurity effect, which may be evident in other measurements that will be performed on this sample. Aside from Laue and μSR, measurements performed in this study produced measurements that are averaged over the bulk of the material, and so they may not show any effect from this impurity. The origin of these impurity peaks are most likely due to elemental Uranium, which shows strong peaks at 34.9°, 35.3° and 36.2° in the α-Uranium phase [64, 65].

Laue diffraction was performed to analyze the crystal quality, and in the hopes of aligning the sample. All of the Laue diffraction measurements in this thesis were performed on a Phillips combined Laue/Gunier camera, with the exception of the Laue measurements on the second UCoGe crystal. This Laue machine uses a white beam of X-rays, with an acceleration voltage of 40kV and a current of 30mA. This resulted in an exposure time of approximately 45 minutes per experiment. The analysis of these Laue patterns were done using OrientExpress software, Version 3.4.

The Laue measurements of the second UCoGe crystal were done using a Tungsten tube source, powered by a Spellman power supply. The acceleration voltage was 10kV, and a current of 12mA. The diffracted X-rays were detected electronically with a Multiwire Laboratories detector, and the data was collected and analyzed using NorthStar data analysis software. The typical exposure times for these experiments were approximately 60 seconds. The orientation of the patterns was fit using the OrientExpress software, Version 3.4.

A Laue pattern for the first UCoGe growth are shown in Figure 4.3.

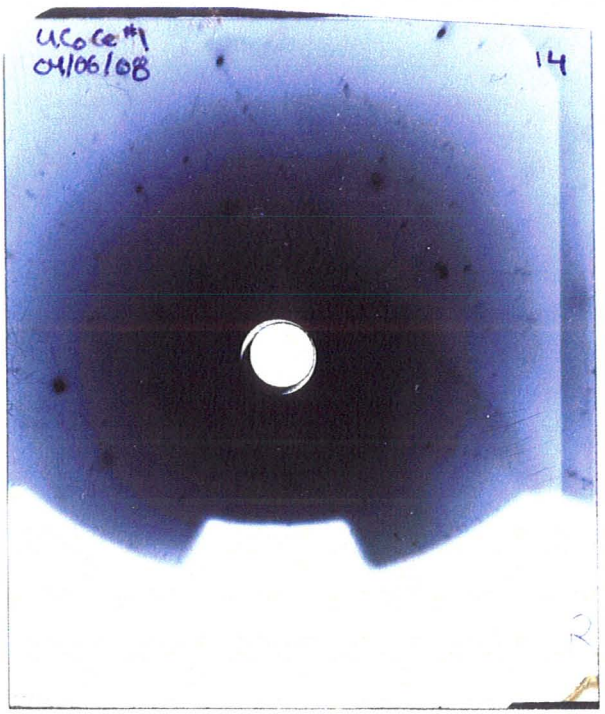

Figure 4.3. A Laue diffraction measurement on the first sample of UCoGe. This shows no obvious high-symmetry points, indicating no dominant grain. The image indicates several grains visible in this area of the crystal. The bright area at the bottom of the image is the sample holder.

This pattern shows that the crystal is polycrystalline, with several grains. This is only a probe of the surface quality, so the bulk may differ in terms of granularity. The grains do not appear to be closely aligned, so aligning this sample was not possible. Attempts to image different areas of the surface showed similar results.

The Laue diffraction patterns for the second growth of UCoGe are shown in Figure 4.4. These show much better quality, since some images show only one grain. In other cases where multiple grains are evident, they appear to be aligned to within 2° (see Figure 4.4*(b)*). This indicates that the pattern could be fit, and the crystal can be aligned. The results of the alignment are shown in Figure 4.5.

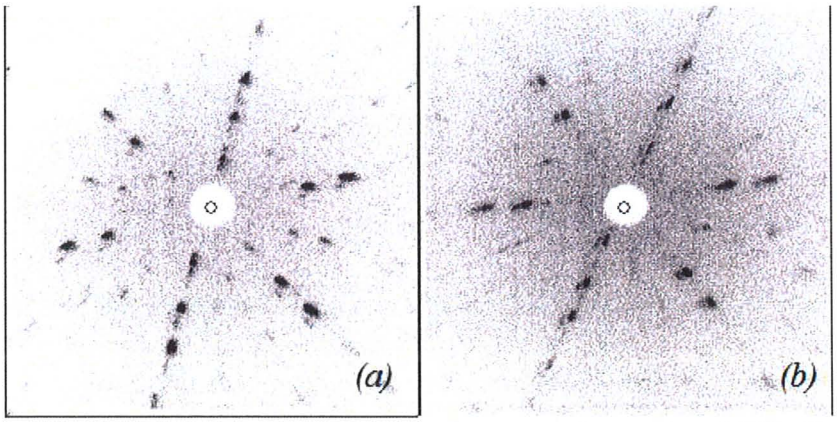

Figure 4.4. The Laue diffraction measurements on the second sample of UCoGe. *(a)* shows a face with only one grain. The high symmetry point in the centre is one of the axes. *(b)*shows part of the same face, at a different location. Here, two grains are observed, but they are very closely aligned.

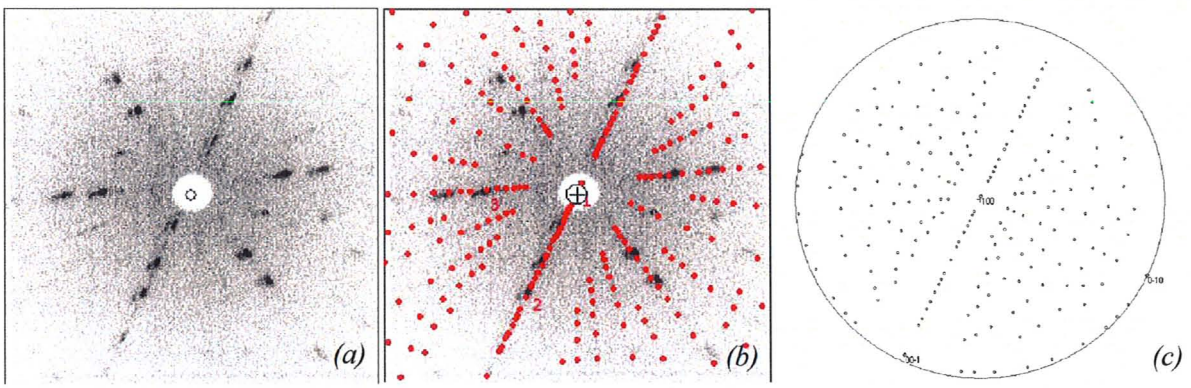

Figure 4.5. The Laue diffraction pattern from Figure 4.4*(b)* is fit with orientation software. This pattern is shown again in *(a)*. *(b)* The calculated points given by the fitting software is indicated by red dots at the calculated locations of the Bragg peaks. This is based on the centre of the image being aligned with the *a*-axis. *(c)* This is the stereoscopic projection of the Bragg peaks based on the fit. This image also shows the positions of the other major axes.

Figure 4.5(*a*) shows that the Laue pattern of the crystal is close to alignment. It also shows the fit given by the OrientExpress V3.4 alignment software, which shows reasonably good agreement. Finally, Figure 4.5(*c*) shows the stereoscopic projection of the crystal based on the fit given in Figure 4.5(*b*). This allows us to determine the angles of the various major axes to the growth direction of the crystal (which is vertical in these images).

Based on this orientation, the crystal was cut by spark erosion such that the *a*-axis was perpendicular to the plane of the cut. This was repeated several times to get several flat plates with this orientation that

could be used for further measurements.

4.2 DC Resistivity

DC resistivity measurements were made on both crystals of UCoGe. The first crystal was measured using a standard He-4 gas flow cryostat, with a base temperature of 1.7K. The resulting measurements are shown in Figure 4.6.

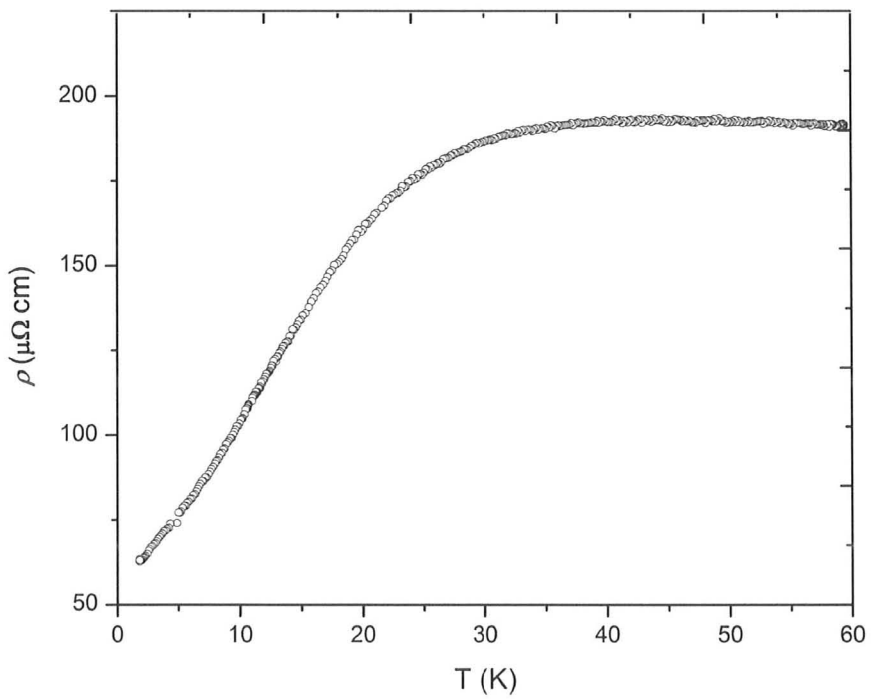

Figure 4.6. The resistivity of the first UCoGe crystal from 1.7K to 60K. We see a continuous downturn, occurring around 30K.

It is evident that the behaviour of this crystal at high temperature is typical of a metal, as the high-temperature resistivity tends to a constant value, while a decrease is seen at low temperature. It is primarily

this low temperature resistivity that determines the crystal quality, since a more uniform (single) crystal will display a very low resistivity at low T. Due to this low resistivity at low T, high quality crystals will display a large residual resistivity.

From Equation (2.1), we can calculate the residual resistivity ratio for this crystal. Using the lowest resistance value and the average resistivity at high T, we obtain a value of RRR=3.5. This is lower than other crystals studied elsewhere [45, 46, 48, 53, 54, 66] where values are reported to be between 10 and 30.

The resistivity measurements on this sample display no changes at low temperature that could be attributed to the ferromagnetic transition. This may be due to the lower sample quality, but the measurements were only performed as low as 1.7K, which is only slightly below the reported value of 2-3K [45]. However, it has been reported that using resistivity to measure the ferromagnetic transition does not show any clear change in slope at T_{curie} by some [46, 54], while others claim to be able to see a change at T_{Curie} [48, 66]. This indicates that even if our sample has a ferromagnetic transition around 2-3K, it may not be identifiable without more measurements below T=1.7K.

The second sample of UCoGe was measured in a dilution refrigerator (DR) at the National High Magnetic Field Laboratory (NHMFL), in conjunction with researchers from Florida State University. The DR has a base temperature of 0.01K, and the superconducting magnets used have a maximum field of 18T. This allows a more thorough analysis of the transport properties of the material around both the ferromagnetic and superconducting transitions. The measured resistivity is shown in Figure 4.7.

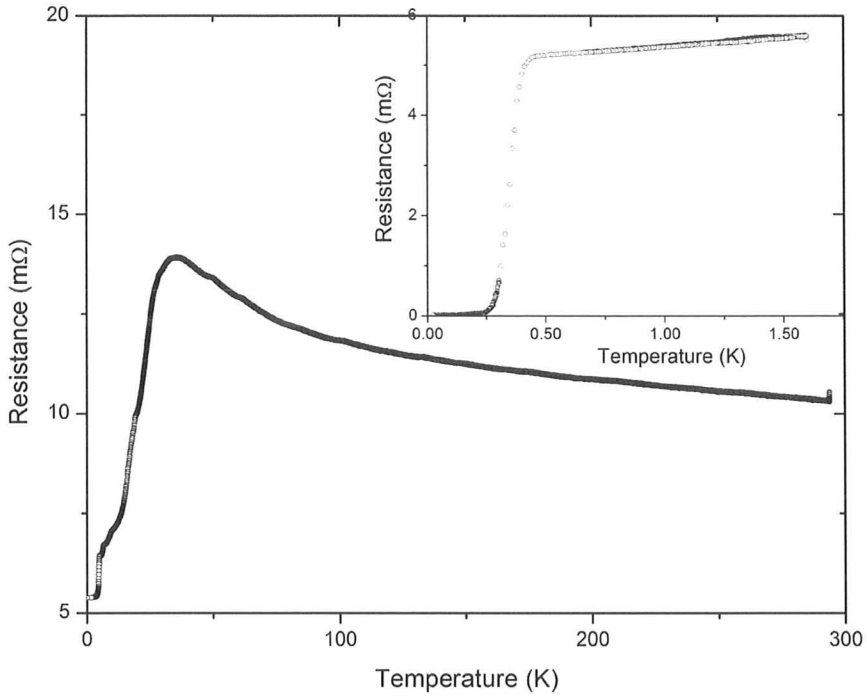

Figure 4.7. The resistivity of the second UCoGe crystal from 0.02K to 300K. The resistance peaks around 40K, then decreases. The drop below 8K is due to instrumentation. *(inset)* The low-T resistance shows the onset of superconductivity at 425mK, and zero resistance below 300mK.

This data, most noticeably, shows that this sample is superconducting, with an onset of 425mK. The sample has zero resistance below 300mK. A peak in the resistance is observed around 40K, after which the resistance decreases as the temperature decreases. A few of the noticeable features below 40K appear as changes in the slope of the line. The most obvious feature is a sharp decrease at 4.5K. This temperature is too high to be attributed to the ferromagnetic transition, and since it also appears in the measurements of URhGe (see Figure 5.9), it is likely due to the apparatus or measurement. Since it is in the region of the Helium phase transition, this drop is probably caused by changes in the cooling rate as the Helium coolant changes from gas to liquid.

Using this data, we can also calculate the RRR of this sample, based on Equation 2.1, yielding a value of approximately 2.5. This is lower than for the first sample, but other measurements of the sample quality

(Laue, etc.) suggest that the second sample is of better crystallinity. The lower value of the RRR may suggest that this crystal has more impurities, leading to scattering. The other advantage to measurements performed on this crystal is that it has been shown to be superconducting, and has well-defined transition temperatures.

The superconducting transition is slightly broadened, but this is not unusual, as such broad transitions have been observed in other studies of these materials [54]. This measurement will now be used as a basis for other measurements on this sample, since the location and width of the superconducting transition is now known.

4.3 Bulk Magnetometry

Bulk magnetometry measurements were performed on both crystals, using the SQUID magnetometer described in Section 2.4. The purpose of these measurements was to study the magnetic behaviour of the samples, and to hopefully observe the ferromagnetic transition. The measurements of the magnetic susceptibility was done in a field of 100 Oe.

The measurement of the magnetic susceptibility of the first UCoGe crystal is shown in Figure 4.8. We see a downturn that may signify the onset of a magnetic transition. However, because of the extremely small moment size in the system, this transition is very weak, and hard to detect. The data was fit to a Curie-Weiss Law, as given in Equation (2.6), plus a constant.

$$\chi_1(T) = A + \frac{C}{T-\theta} \qquad (4.1)$$

The fit to this function is shown in Figure 4.8, and gives the values $A = 2.9989 \cdot 10^{-4} \pm 0.0671 \cdot 10^{-4}$ emu,

$C = 0.00487 \pm 0.00007$ emu·K, and $\theta = 1.984 \pm 0.021$ K. Since the transition is very weak in this sample, this type of fit may not yield an exact value, but it does agree well with the data. Other measurements are needed to verify if there is a magnetic transition at this temperature.

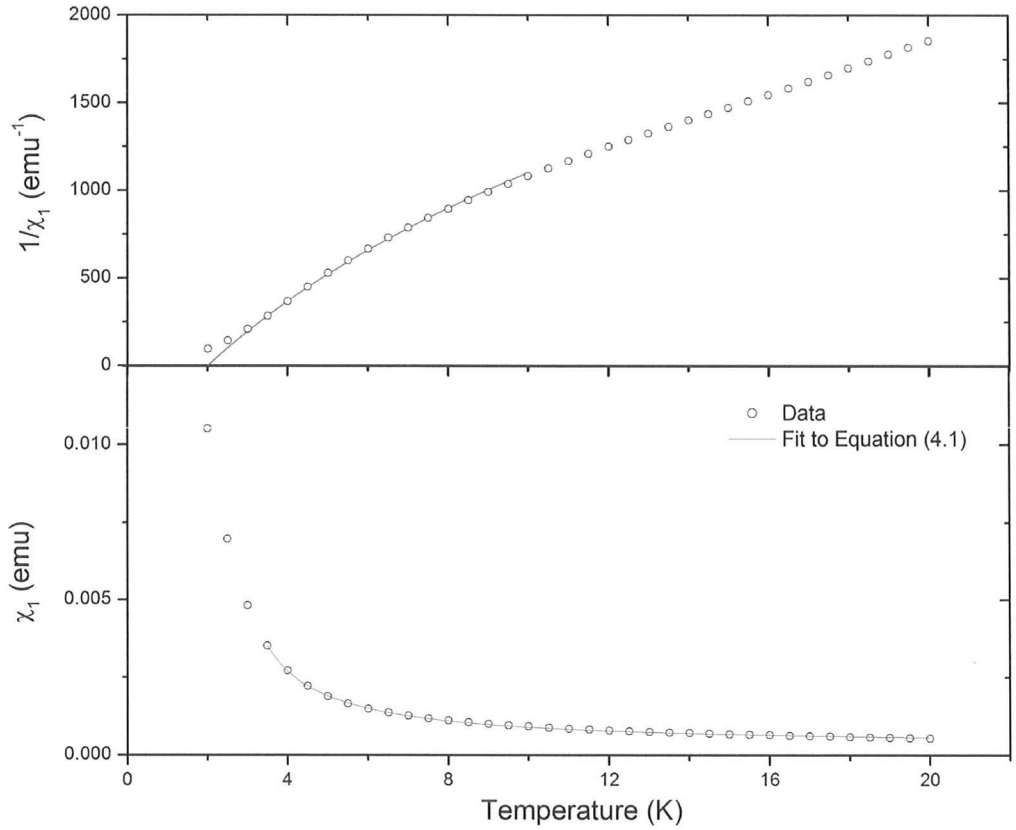

Figure 4.8. Magnetic susceptibility, χ_1, versus temperature for the first UCoGe crystal. A slight downturn is observed below 5K, which may indicate the proximity to a magnetic transition. The fit to Equation (4.1) gives good agreement to the data, and yields a value of $T_{Curie} = 1.98(2)$K.

The second measurement that was done in the SQUID magnetometer on this sample was a hysteresis loop at 1.7K. This involves sweeping the field from a negative value to a positive value, and back again, measuring the magnetization of the sample. In a magnetically ordered material, the sample orders in the field. Lowering the field will offset the magnetization due to remnant flux density within the material [67]. The hysteresis measurement is shown in Figure 4.9.

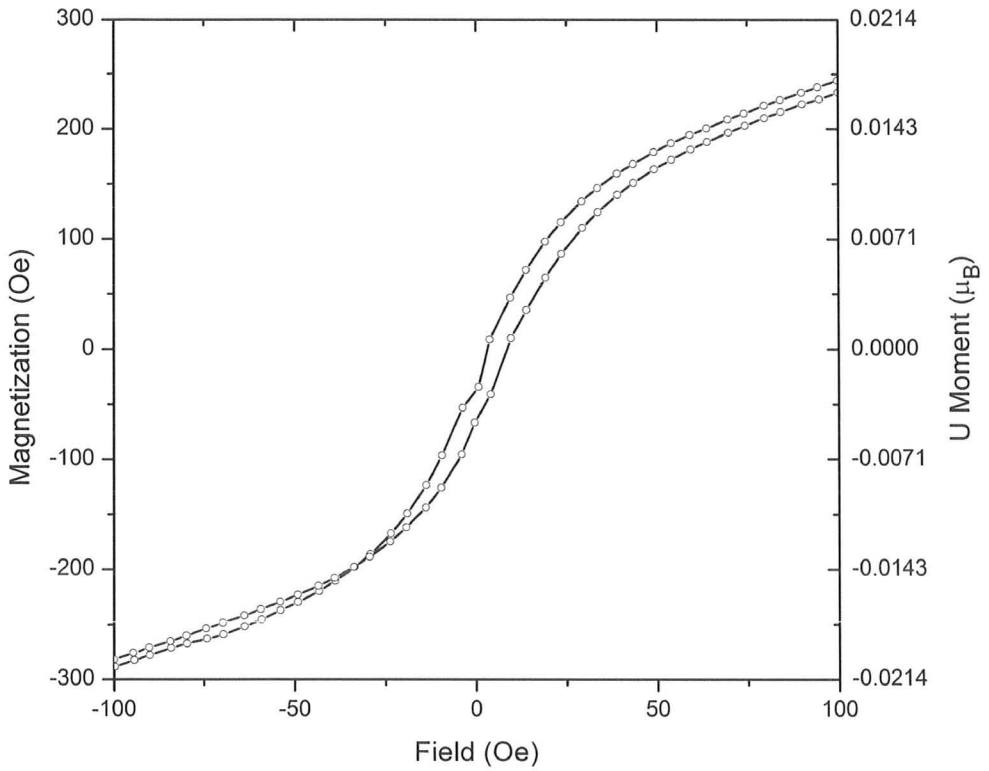

Figure 4.9. Hysteresis loop in the first UCoGe sample, done at T=1.7K. This loop is slightly open, indicating soft ferromagnetic order.

This shows a slightly open loop, indicating that the material is magnetically ordered at T=1.7K. The magnetization data indicated a magnetic transition at T=1.98K, which is above this point. Thus, the open hysteresis loop is confirmation of the fit, and a value for T_{Curie} = 1.98(2)K. Since the loop is only slightly open, it indicates that the remnant flux in the material is small. This soft ferromagnetism is likely an intrinsic property of the material. The observed situation will be further studied by μSR, which can be used to measure magnetic volume fractions. This will be discussed in more detail in Section 4.4.

The second UCoGe sample was also measured in the SQUID magnetometer. The temperature dependence of the magnetization is shown in Figure 4.10.

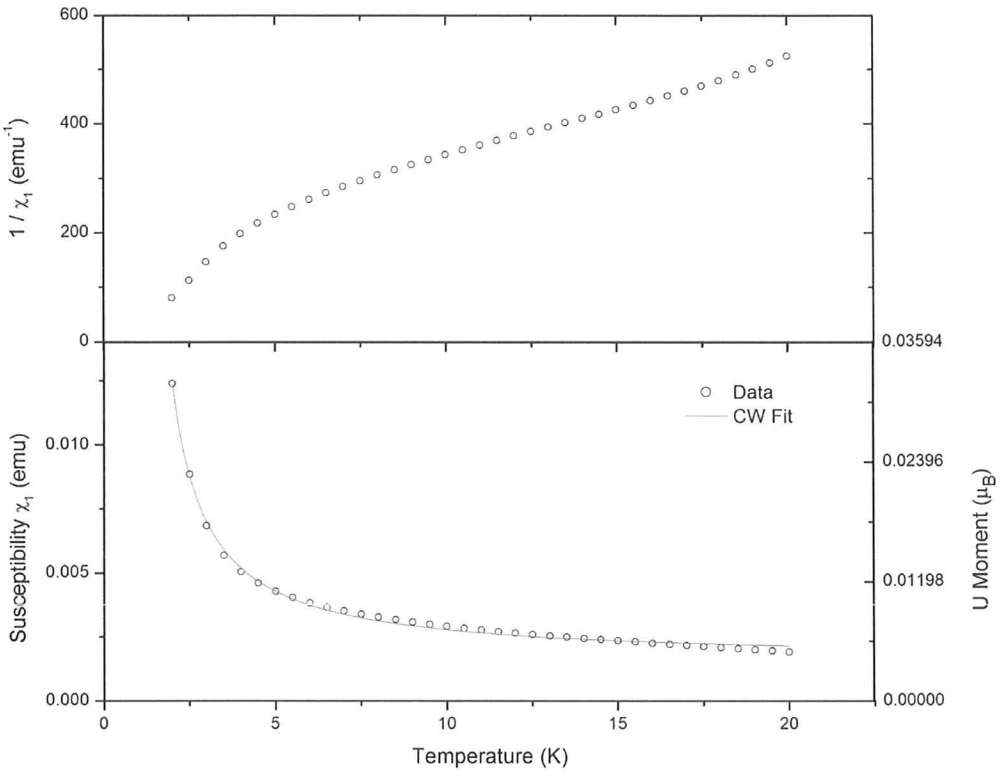

Figure 4.10. Magnetization and U Moment size versus temperature for the second UCoGe crystal. The upturn indicates the onset of a magnetic transition, though data below 1.7K is needed to fill in this transition. The U moment size is smaller than indicated elsewhere, though the low-T data is needed to find the saturated moment. This was fit to Equation (4.1), giving $T_{Curie} = 0.99(3)$K.

The increase in the magnetic susceptibility below 5K is indicative of the proximity to a magnetic transition. The effective U moment size is increasing as the moments become polarized, but there is no indication of any saturation of the effective magnetic moment above 1.7K. This was also fit to Equation (4.1), and the fit is shown in Figure 4.10. The Curie temperature from this fit was found to be 0.995 ± 0.034K. With the fit to Equation (4.1) in Figure 4.10 giving $T_{Curie} \sim 1.0$K, this increase in the susceptibility without any saturation is what should be expected.

If $T_{Curie} = 1.0$K, then a rough extrapolation of the data in Figure 4.10 would give a saturated moment size of approximately $0.05\mu_B$ near T=0K, which is slightly higher than the ordered moment of $0.03\mu_B$

reported in other studies [45, 48]. This may be due to impurities, but is unlikely to be caused by elemental Uranium impurities, since the ordered moment of α-Uranium at 2K is only $0.04\mu_B$ [68]. This question can be better addressed with higher quality samples.

4.4 μSR

The two UCoGe samples were studied by μSR at TRIUMF, on the M20 and M15 beamlines. M20 is a surface muon beamline with a temperature range of 1.7K to 300K. M15, for our measurements, used a dilution refrigerator to allow measurements as low as 20mK. Measurements of these two samples were performed on both beamlines, and the measurements related to each will be noted.

Both Zero-Field (ZF) and Transverse Field (TF) μSR measurements were performed on both samples. An example of the ZF-μSR spectrum at 1K and 5K for the second UCoGe sample is shown in Figure 4.11.

Here, a small oscillation is observed in the 1K data, due to the magnetization of the sample. The ferromagnetism causes this precession due to the internal field at the muon site. However, this precession quickly decays, indicating that the magnetic field distribution is fairly inhomogeneous. The data can be fit, though with only 1 to 1½ periods of the oscillation, the fits will not be as accurate as in the case of URhGe (to be discussed in Section 5.4).

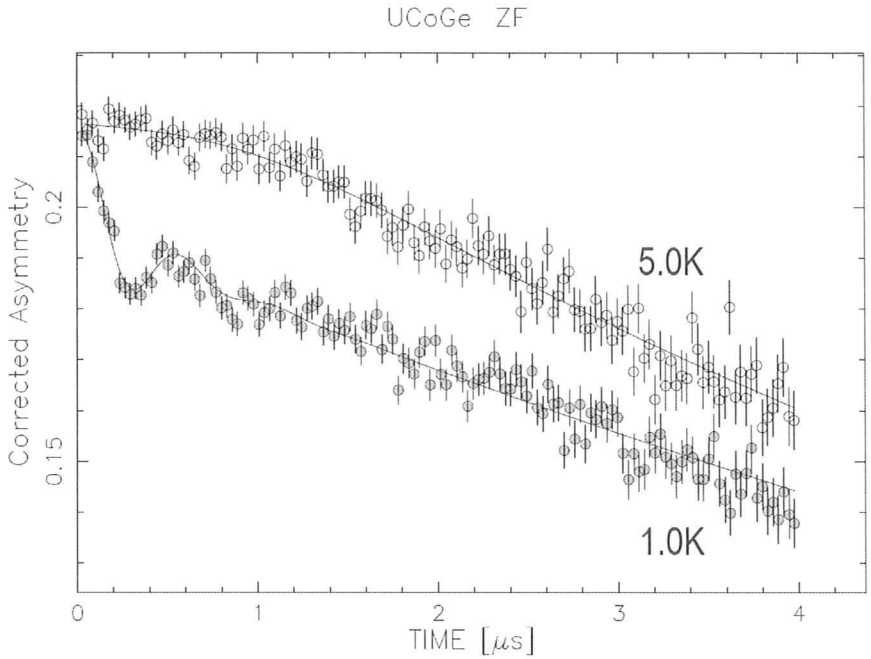

Figure 4.11. ZF-μSR spectra of the second UCoGe crystal at 5K and 1K. The spectrum at 5K is characteristic of paramagnetic behaviour, while the lower spectrum is indicative that the sample is in the ferromagnetic state at 1K.

The data was fit to the function,

$$A(t)=A_S\exp(-\Lambda_S t)\cos(\omega t+\theta)+A_E\exp(-\Lambda_E t)+A_B \qquad (4.2)$$

where A_S, A_E, and A_B are the sample, Exponential and background asymmetries respectively, Λ_S is the sample relaxation rate, Λ_E is the Exponential relaxation rate, ω is the precession frequency, and θ is the phase of the polarization. The extra background term, A_B, is used to account for the background signal produced by the dilution refrigerator.

Using this fitting function, the data was fit to obtain the plot shown in Figure 4.12. This fit is in good agreement with the data, with a reduced χ^2 = 1.676 at 20mK, and a smaller reduced χ^2 at higher temperatures. Plotting the frequency of the oscillation versus temperature, we obtain the plot in Figure 4.13.

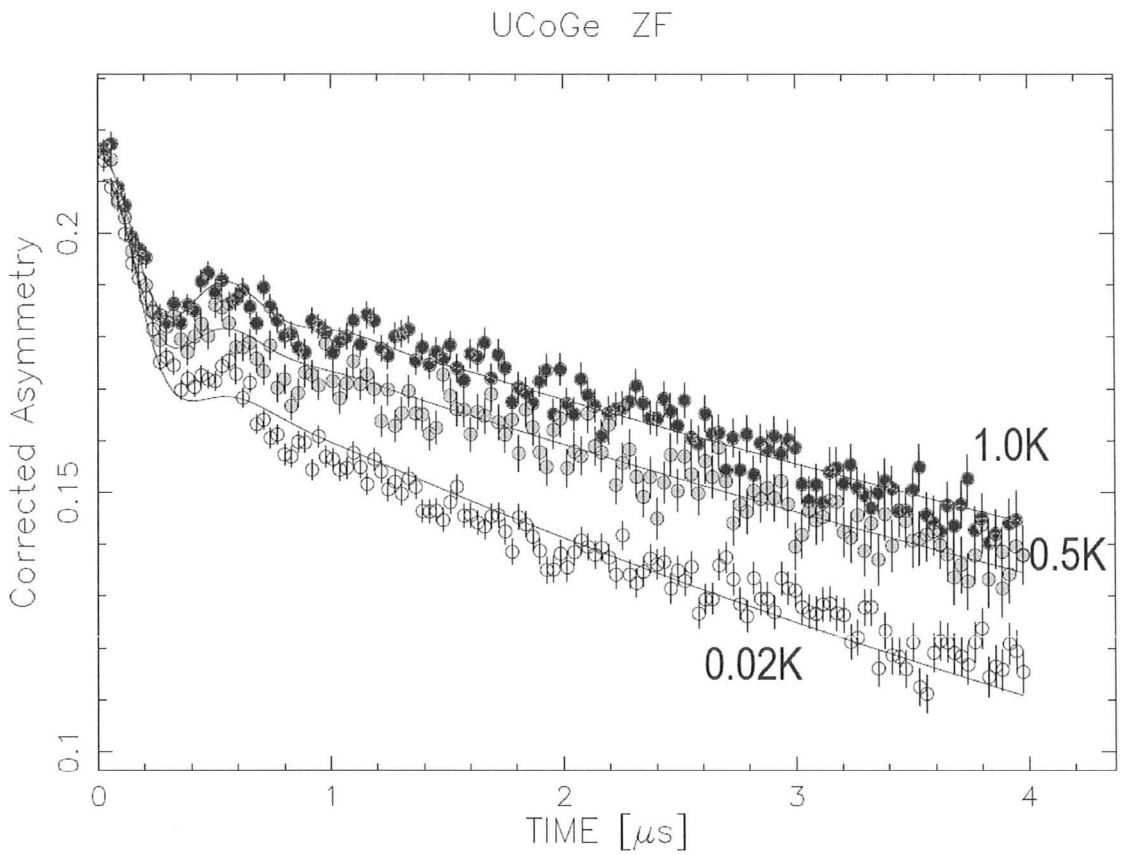

Figure 4.12. ZF-μSR spectra of the second UCoGe crystal at 1K, 0.5K and 20mK, fit to Equation (4.2). The amplitude of the oscillatory signal decreases in the superconducting region, while the frequency also drops by ~10%.

Very clear evidence is seen for the transition at T_{Curie}. Above the Curie temperature, the frequency drops to zero, since the material is in the paramagnetic state. The μSR measurements find that the ferromagnetic transition is at T = 1.7K, slightly higher than in the susceptibility measurements. The frequency increases below this temperature, approaching 1.9MHz at 0.5K. Using Equation (3.8), we can find the internal field by,

$$H_{loc} = \omega / 135.54 \frac{MHz}{T} \qquad (4.3)$$

A frequency of 1.9MHz corresponds to an internal field of approximately 0.014T at the muon site. The onset of the ferromagnetic transition is more gradual than in the URhGe case, which can be ascribed to

the weaker moments in this system. Equation (4.2) was used to fit all of the data points, and the frequency was allowed to be any value, even above T_{Curie}. As can be seen from Figure 4.13, the frequency found from the fits decreases to zero above T_{Curie}, but it more broad than in the case of URhGe.

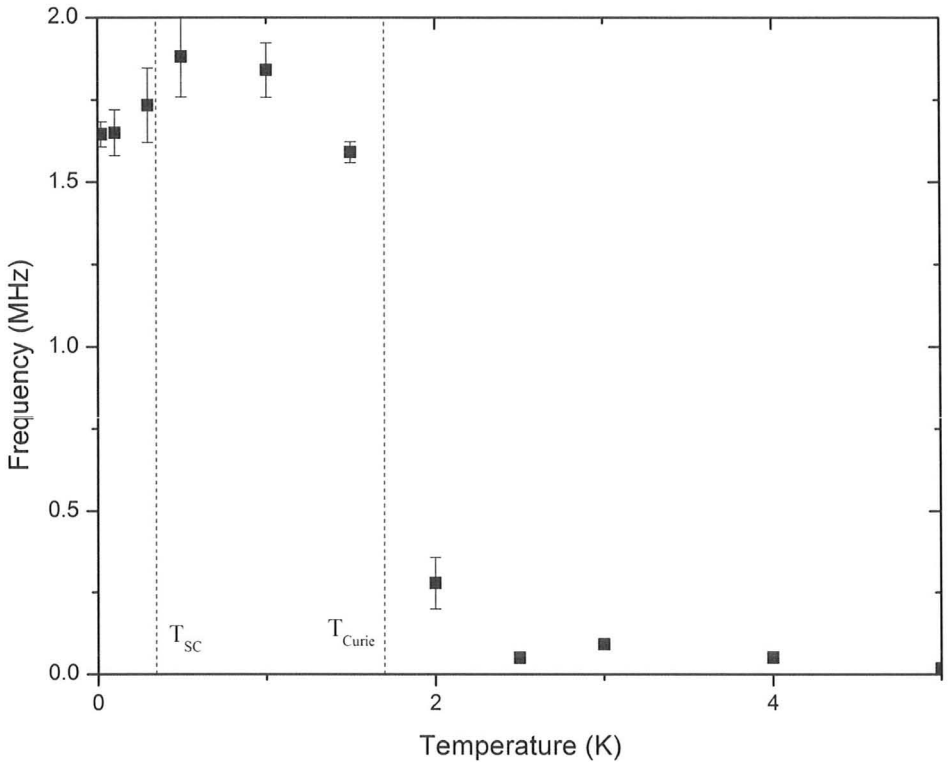

Figure 4.13. Frequency versus temperature in the ZF-μSR spectra of the second UCoGe crystal, from 20mK to 5K. We see that above T_{Curie}, the frequency fits to a value of approximately zero, with an increase to 1.9MHz between 0.5K and 1.5K, characteristic of ferromagnetism. Below T_{SC}, the frequency drops by ~10%.

Using the μ^+ site calculated in [54], we can find that the moment size in the system corresponds to $m_0 = 0.065\mu_B \parallel \hat{c}$, in reasonable agreement with our magnetometry measurements, which found a moment size of $m_0 = 0.05\mu_B$. Below the superconducting transition, the internal field decreases by ~10%. More measurements would help to clarify this transition, but this is an obvious change between 0.02K and 0.5K as seen in Figure 4.11, corresponding very well to the transition seen by resistivity measurements. This is also a larger change than observed by other μSR measurements on UCoGe [54].

The relaxation rate of the μSR spectra is shown in Figure 4.14.

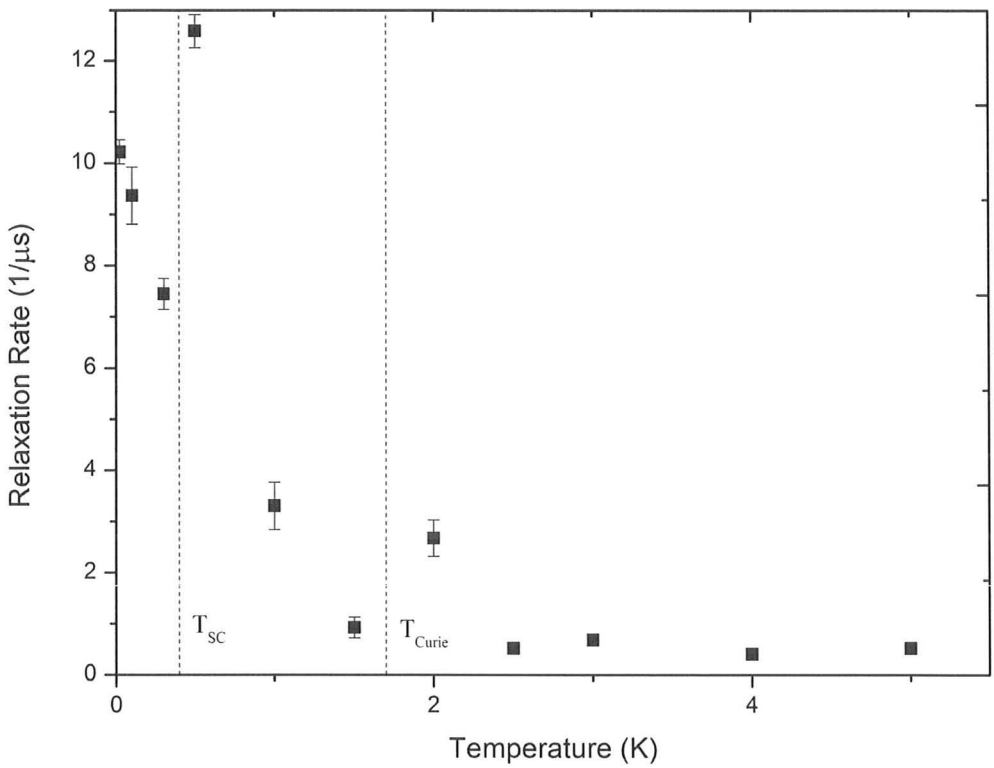

Figure 4.14. ZF-μSR plot of Relaxation versus Temperature in the second UCoGe crystal. The relaxation rate increases below T_{Curie}, decreases sharply at the superconducting transition, then increases towards T=20mK.

The relaxation rate is small above the ferromagnetic transition. Below the transition, the relaxation rate increases, indicating an increase in the coupling between the ferromagnetic moments and the muon moments. Just above the superconducting transition, the relaxation rate peaks, and shows a sharp decrease across the superconducting transition. The relaxation rate then increases as the temperature decreases.

We also measured the second UCoGe sample in several TF-μSR measurements, some of which are shown in Figure 4.15. We began by measuring the sample in a TF of 200G, while cooling the sample to 20mK in zero applied field. The plot of frequency versus temperature is shown in Figure 4.16, and the plot of relaxation versus temperature is shown in Figure 4.17.

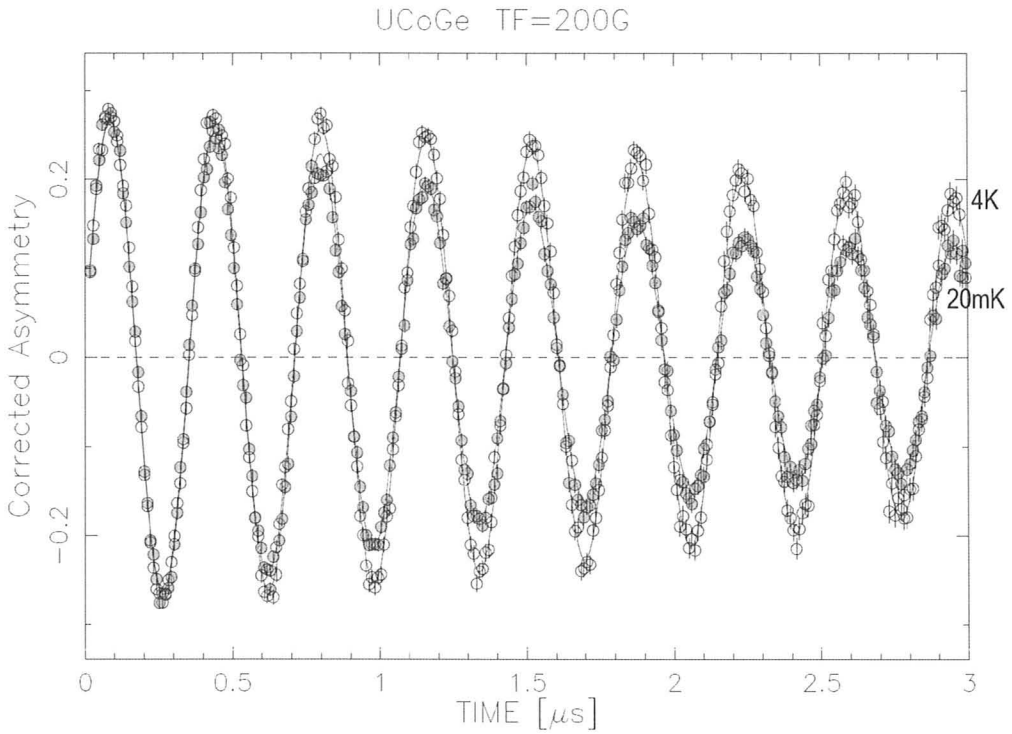

Figure 4.15. The TF-μSR spectra of the second UCoGe crystal in an applied field of 200G, shown at 4K (open circles) and 20mK (filled cirlces). We see an increased relaxation with decreasing temperature.

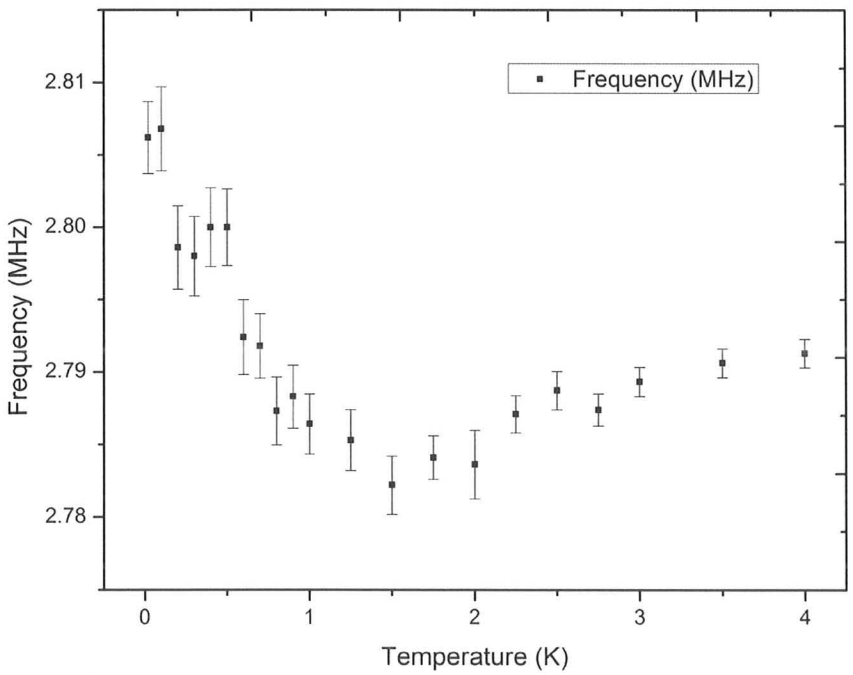

Figure 4.16. TF-μSR plot of Frequency versus Temperature in the second UCoGe crystal. The measurements were done in an applied field of 200G, while cooling the sample in zero applied field. This displays no clear indication of superconductivity.

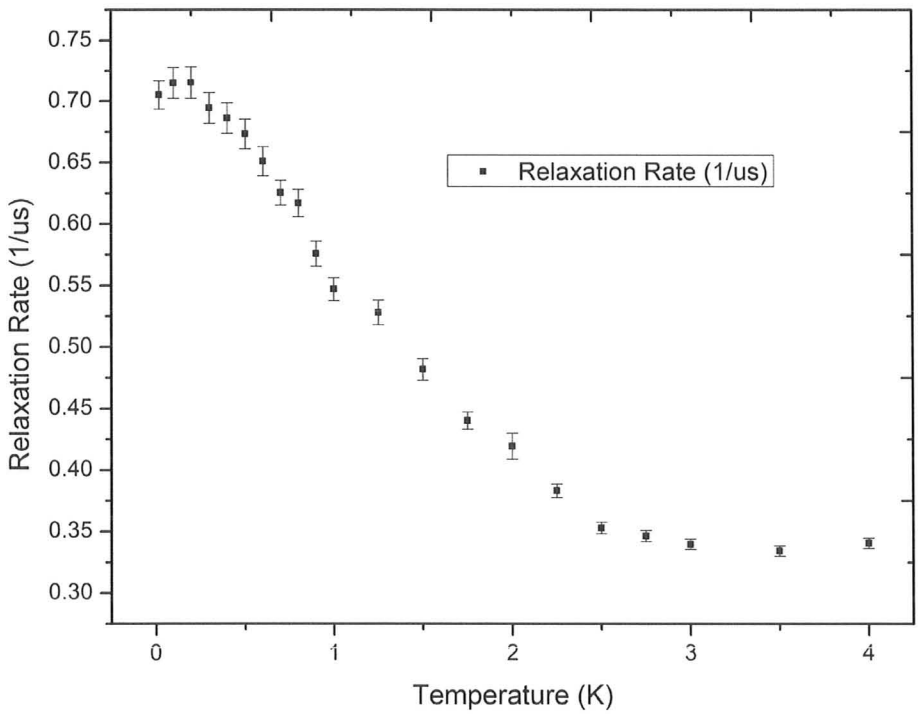

Figure 4.17. TF-μSR plot of Relaxation versus Temperature in the second UCoGe crystal. The measurements were done in an applied field of 200G, while cooling the sample in zero applied field. From these measurements, T_{Curie} appears to be approximately 2.5K.

In Figure 4.17, the relaxation is constant above 2.5K. Below 2.5K, the relaxation increases down to 200mK, where the relaxation seems to saturate. This would suggest a Curie temperature of 2.5K, which is much higher than that found by ZF-μSR and with susceptibility measurements. This may be due to a broad transition, which was seen with ZF-μSR.

The saturation in the relaxation rate at low temperature is an indication that the full volume fraction has ordered. This appears to be the case below 300mK, indicating that the saturation occurs just above the superconducting transition.

4.5 Conclusions

The two crystals of UCoGe were analyzed using multiple techniques. The structure characterization measurements showed that the samples were polycrystals of the correct phase. The Laue measurements, as well as the resistivity measurements showed that the second growth was of better quality than the first growth. The second crystal also displayed Laue patterns that allowed the sample to be oriented with a moderate degree of accuracy.

The resistivity measurements do not display clear evidence of the ferromagnetic transition, but this is not surprising due to the small moment size in the system. This weak signal in the resistivity measurements has been observed previously [45, 48, 66].

The resistivity measurements performed on the second UCoGe crystal at NHMFL show that this sample is superconducting, with $T_{SC\rho=0}$ = 300mK. This measurement will prove important when performing μSR measurements to identify any changes that may occur around the superconducting transition.

The SQUID measurements support the idea of small moments, ferromagnetically ordered in this system. The hysteresis loop in Figure 4.9 has a very small area, and the ferromagnetic transition in Figure 4.8 is broad, and involves a small magnitude change in the magnetization. The broadness of the transition seem to be intrinsic to the system [45, 48, 66], and not a result of impurities, or domain boundaries. The close agreement of the magnetization measurements to measurements previously reported is further evidence that we have obtained crystals with similar properties.

The ZF-μSR measurements show a ferromagnetic signal below 2K. This signal relaxes rapidly, which may be a sign of slowing ferromagnetic fluctuations, which depolarize the muon spins. The onset of the

ferromagnetic signal is fairly broad, with measurements at 2K showing a small degree of oscillation. We expect that this is due to small moments, and impurities in the system, since the ferromagnetic transition has been reported to be as high as 3.5K [45, 48]. However, the μSR and magnetometry measurements agree on a ferromagnetic transition around T = 1.7K in the second UCoGe sample. From the TF-μSR measurements, we also see that the magnetic volume fraction continues to increase below T_{Curie}, and the ZF-μSR shows a broad internal field distribution, both of which may increase the error in measuring the ferromagnetic transition.

We see a large drop of ~10% in the frequency measured by μSR below T_{sc}. This is in contrast to other published results [54], which report a decrease of approximately 2%. At this stage, a definitive reason for the disagreement in this value is unclear, but it may be due to variations between sample. This may also be due to differences in the fitting procedure used in this study and elsewhere [54], though this difference is only slightly outside of the error bars.

The TF-μSR measurements suggest a ferromagnetic transition around 2.5K, which is higher than that found by ZF-μSR and susceptibility. The SQUID measurements show a very broad transition, and thus it may be easier to see the onset of the transition in the TF-μSR signal.

There is also no signature of superconductivity in the TF-μSR measurements. If the volume fraction is on the order of 2%, as reported elsewhere [54], then this may be hard to resolve. However, the ZF-μSR show that the transition is there. As in the case of other heavy fermion compounds, these materials would have a large penetration depth, and thus the contribution of the superconductivity to the relaxation rate should be small. As such, it may be below the resolution limit of our measurements. Measurements in the future should focus on better quality samples, with longer measurements to reduce noise, and make any signature of the transitions more apparent in both ZF and TF-μSR.

V. Measurements of URhGe

5.1 Structure Characterization

Two growths of URhGe were done, under the conditions described in Section 2.1. In addition to Laue and powder X-ray diffraction measurements, Scanning Electron Microscopy measurements were done to characterize the structure. A Laue diffraction image from the first URhGe crystal is shown in Figure 5.1.

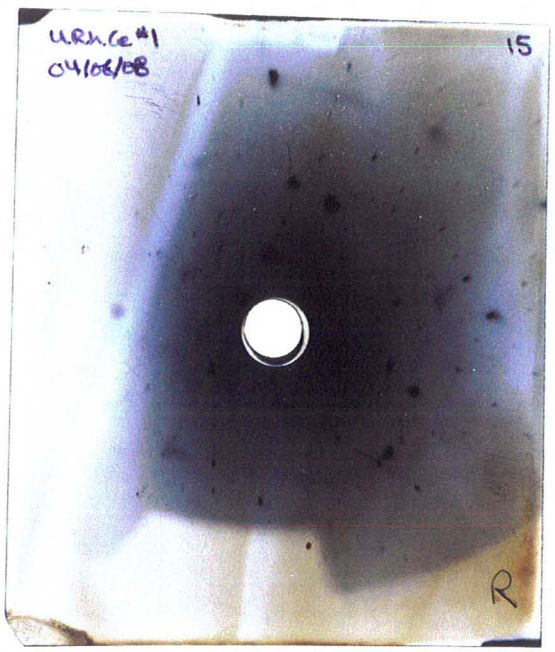

Figure 5.1. A Laue diffraction measurement on the first sample of URhGe. A symmetry point is visible on the lower left of the image. Some of the points, particularly those above the centre, indicate multiple grains. The bright area in the bottom of the image is the sample holder.

It can be seen from the diffraction pattern that this is a polycrystal, which has multiple grains with random orientations. As such, this crystal was not suitable for orientation, but it may be possible to separate small single crystals for measurements only requiring samples of that size, such as transport measurements.

Figure 5.2 shows Laue diffraction images from the second growth of URhGe.

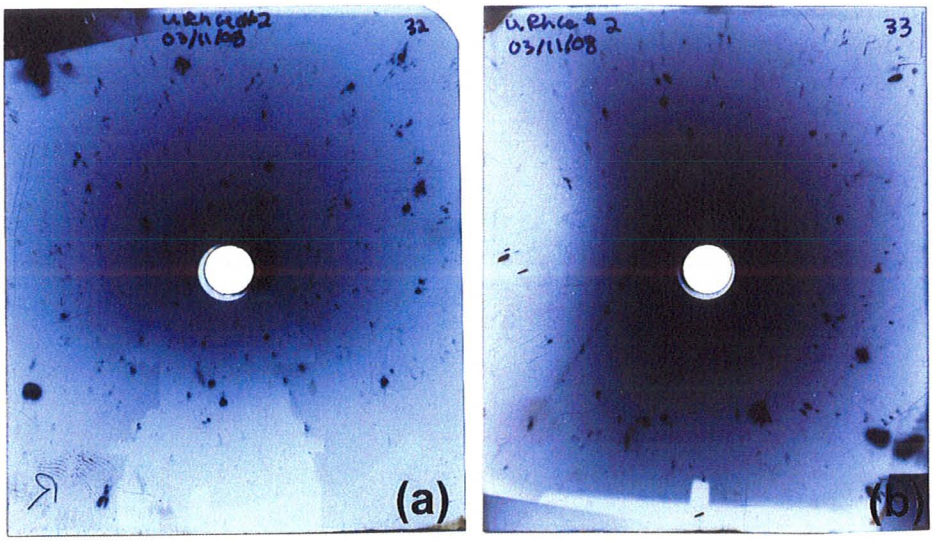

Figure 5.2. The Laue diffraction measurements on the second sample of URhGe. Both images were taken at the terminal end of the growth, at a point where the crystal had broken. *(a)* is taken parallel to the growth axis, while *(b)* was taken perpendicular to the broken face. Both images show multiple grains in the crystal.

These also appear to be polycrystalline, but of slightly better quality than the first growth. Since these crystals were grown at nearly the same time, the remainder of the measurements were carried out using the second crystal of URhGe. Powder X-ray diffraction measurements were also done, and these are shown in Figure 5.3.

The powder pattern has not been documented in the literature, or calculated. This made comparing the data to the pattern of a known sample impossible. The lattice constants in Table 1.4 were used with the Wyckoff positions for UCoGe [51] to produce a possible powder diffraction pattern for URhGe, which is shown in Figure 5.4.

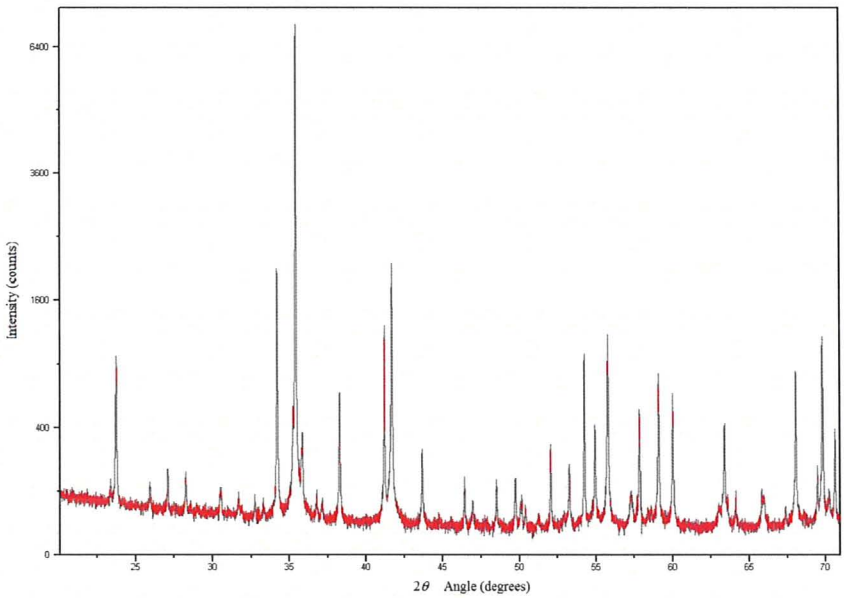

Figure 5.3. The powder X-ray measurements for the second growth of URhGe. This is plotted as a semi-log plot. Some small impurity peaks are noticeable.

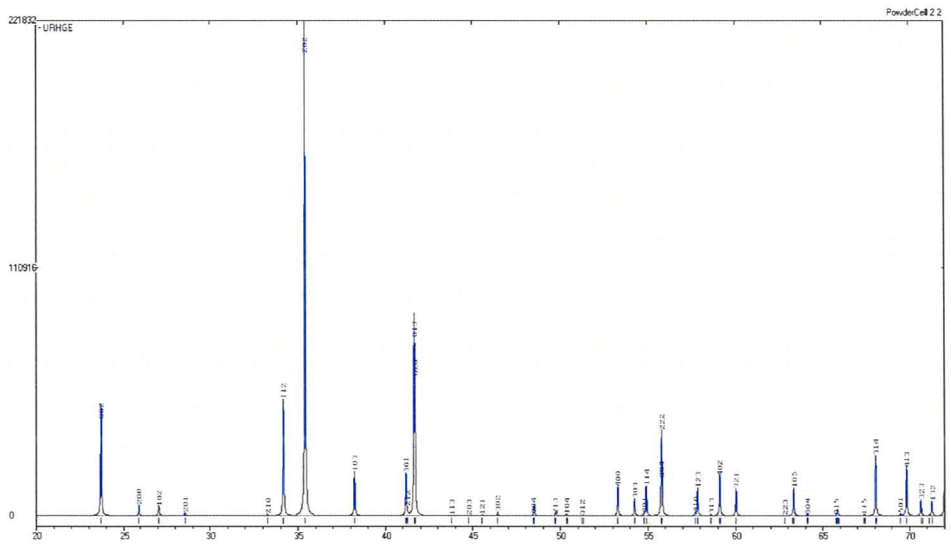

Figure 5.4. The theoretical powder X-ray diffraction pattern for URhGe, based on the lattice constants in Table 1.4 and the Wyckoff positions of UCoGe from [51]. This pattern agrees very well with the experimental pattern in Figure 5.3.

This pattern is very similar to the experimental pattern shown in Figure 5.3. This is understandable, since UCoGe and URhGe are structurally and electronically identical, and so the differences in the Wyckoff

positions should be small.

Comparing this to the experimental pattern in Figure 5.3, we see remarkably good agreement. Some additional peaks are observed, particularly around 23° and 36°, which we attribute to impurities in the sample. The height of the 36° impurity peak to the height of the 35.5° peak in the sample is less than 5%, which is slightly better than in the case of UCoGe. Like the powder pattern for UCoGe, these impurity peaks are most likely due to elemental Uranium, which shows strong peaks at this scattering angle.

While this method does not conclusively prove that the material we have grown is the correct phase, it is very strong evidence in favour of it. Combined with the other measurements to be discussed later in this chapter, we are confident that we have a polycrystal of URhGe in the correct phase. Additionally, since the level of impurities is lower in this sample than in the first growth of UCoGe, we have our first indication of the quality of these samples. This will be discussed further in Section 5.2.

An additional SEM measurement was performed to characterize the structure of this crystal. The motivation for performing these measurements came from the crystal growth. A second phase appeared to be forming in the melt, and solidifying on the surface of the grown crystal. The crystal was annealed after the growth, but we felt that it was important to analyze the surface of the crystal.

This was first done with Laue X-ray diffraction. This image is shown in Figure 5.5, below. This clearly shows powder rings, indicating that the material on the surface is not part of the interior of the crystal. The phase that is on the surface contains a large number of polycrystals, with random orientation. However, the Laue diffraction data does not indicate the constituents of the surface material. For this reason, the SEM measurements were done.

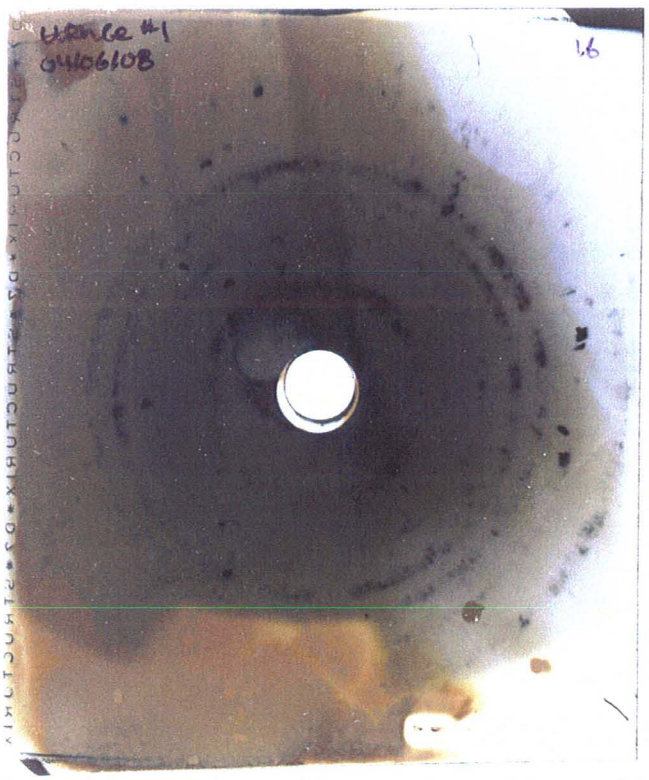

Figure 5.5. The Laue diffraction measurements on the surface of the first URhGe growth. This clearly shows powder rings, indicating that the surface of the crystals are not crystallographically similar to the interior of the crystal. This prompted the SEM analysis.

The SEM image is shown in Figure 5.6. A separate phase is observed that covers the surface of the crystal to a depth of approximately 1-2μm. This is clearly not part of the interior of the crystal.

Electron Probe Micro-Analysis (EPMA) was done to identify the elemental constituents of the surface coating. The EPMA patterns of both the bulk and the surface are given in Figure 5.7.

Figure 5.7*(a)* shows that the bulk of the material contains U, Rh, and Ge. In *(b)*, the surface spectrum, only U and Ge are present, and the Rh peaks are absent. Normalizing this data by the electron cross-sections, we find that U and Ge exist in the surface coating in approximately equal atomic amounts. This indicates that the material on the surface is UGe, or a material with similar stoichiometry.

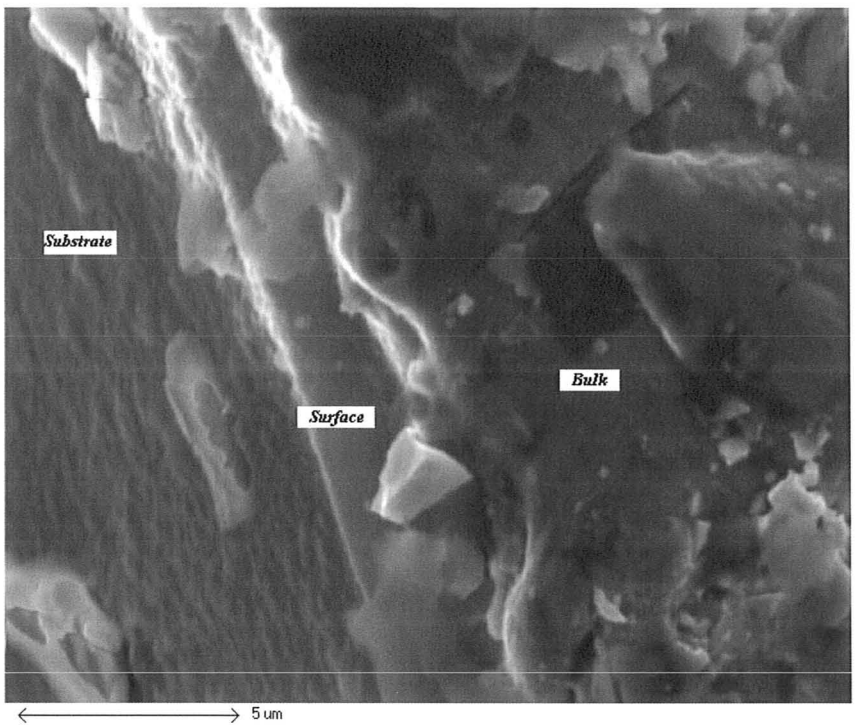

Figure 5.6. The SEM image of the surface of the URhGe crystal. There is a second phase on the surface, ~1-2μm thick. This image is approximately 5950x magnification.

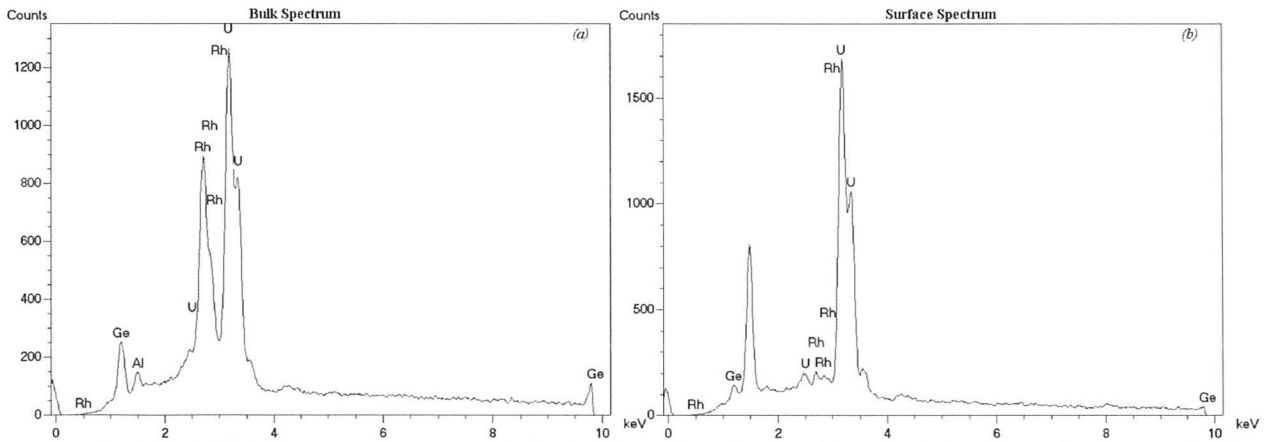

Figure 5.7. The EPMA measurements of the bulk and surface of the URhGe crystal. *(a)* The bulk spectrum shows the presence of U, Rh and Ge. *(b)* The surface spectrum shows the absence of Rh peaks, and U and Ge in approximately equal amounts.

Since the coating is so thin compared to the thickness of the crystal (~5mm), we know that this surface impurity contributes less than 1% or the crystal volume. For measurements such as bulk magnetometry and resistivity, it should not affect the results, unless this impurity is superconducting.

5.2 Resistivity

Resistivity measurements were performed on the second growth of URhGe. The results are shown in Figure 5.8.

Using Equation (2.1), the residual resistivity ratio of the crystal was calculated. Using the resistivity at 1K and 300K, we find that $RRR = 10$ for this crystal. This is comparable to values reported in other samples of this material [38, 39, 42, 52].

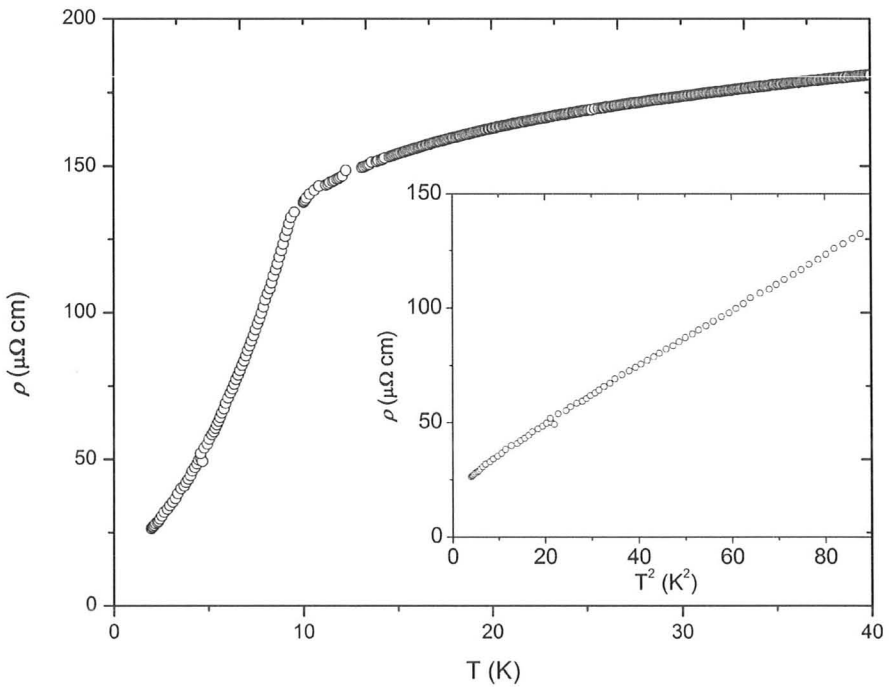

Figure 5.8. The resistivity of the second URhGe crystal from 1.7K to 60K. We see the onset of ferromagnetism at T=9.5K. The resistivity follows $\rho \alpha T^2$ below the transition. *(inset)* The resistivity below 10K is plotted against temperature squared, and it can be seen that the resistivity is linear in T^2.

There is a clear transition in the material at 9.5K. Below this temperature, the resistivity follows the form,

$$\rho \propto T^2 \qquad (5.1)$$

This is expected to be the case in a material which is free from magnetic scattering, and the material behaves as a Fermi liquid, where there is only electron-electron scattering. This indicates that the material is magnetically ordered below 9.5K, which is identified with the transition to a ferromagnet. The combination of the resistivity and bulk magnetometry measurements detailed in Section 5.3 allows us to show that in this crystal, $T_{curie} = 9.5K$.

The sample from the second URhGe growth was studied at low temperatures by researchers at Florida State University, using a DR at NHMFL. The results of these measurements are shown in Figure 5.9.

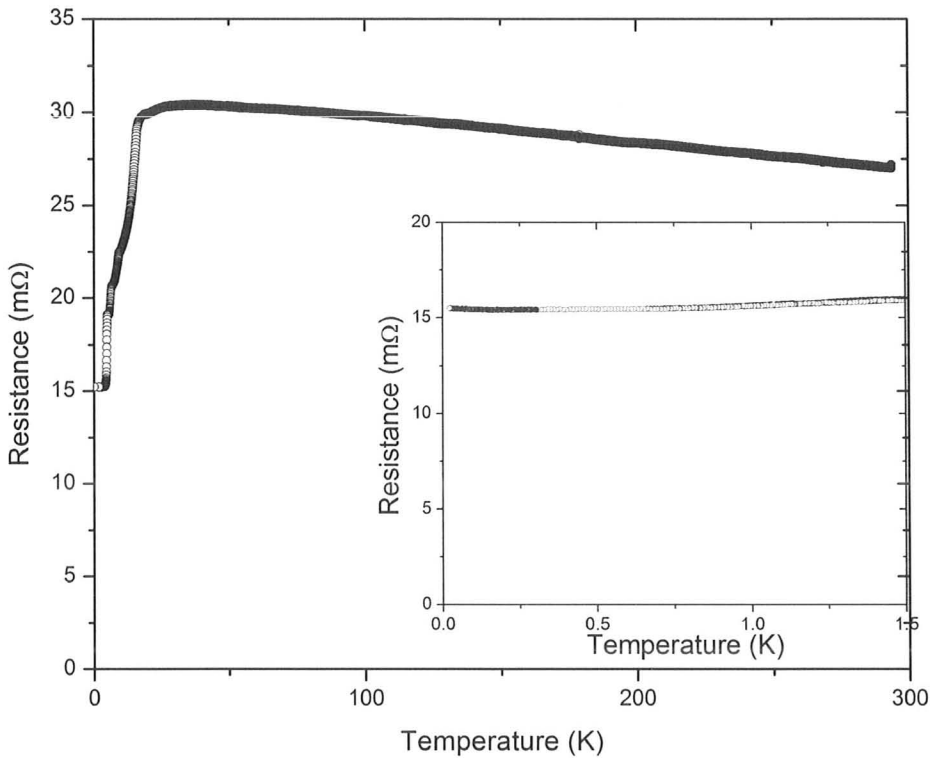

Figure 5.9. The resistivity of the second URhGe crystal from 0.02K to 300K. We see the onset of ferromagnetism at T=9.5K. Another sharp change is seen at 4.5K, but this is likely due to instrumentation. *(inset)* The resistivity of the URhGe crystal below 1.5K. No evidence of superconductivity appears down to 0.02K.

The measurements show no sign of the superconducting transition, down to 0.02K. The ferromagnetic transition is seen at 9.5K, in agreement with the previous measurements performed on the same sample.

There is another noticeable drop seen at 4.5K, which was present in the UCoGe (see Figure 4.7). This indicates that this drop is due to instrumentation, since it was not seen in the previous measurement of this sample. As in the case of UCoGe, this is due to the change in cooling rate in the proximity of the He phase transition.

The result of this measurement is that we know that this sample is not superconducting, and we should not expect to see any signatures of this in other measurements using this sample.

5.3 Bulk Magnetometry

Bulk magnetometry measurements were performed on the second growth of URhGe. The plot of magnetization versus temperature is shown in Figure 5.10.

The data displays a clear transition at 9.5K. This is attributed to the ferromagnetic transition, where the moment size saturates toward T = 0K. Extrapolating the data, we see that the moment size saturates at $m_0 = 0.37\ \mu_B$. This is slightly lower than the values for URhGe given elsewhere [35, 38, 39, 41, 44]. This may be due to the sample quality, since our RRR appears to be lower than that reported elsewhere.

A hysteresis loop was also measured at T = 1.7K, shown in Figure 5.11.

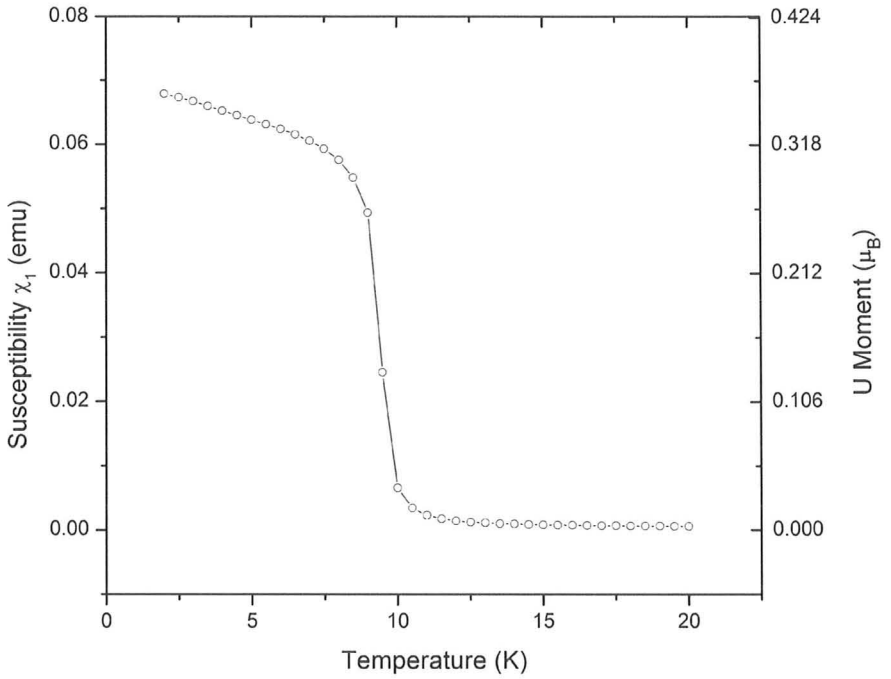

Figure 5.10. Magnetization and U moment size versus Temperature. A clear ferromagnetic transition is seen at 9.5K, and the moment size agrees fairly well with values reported elsewhere.

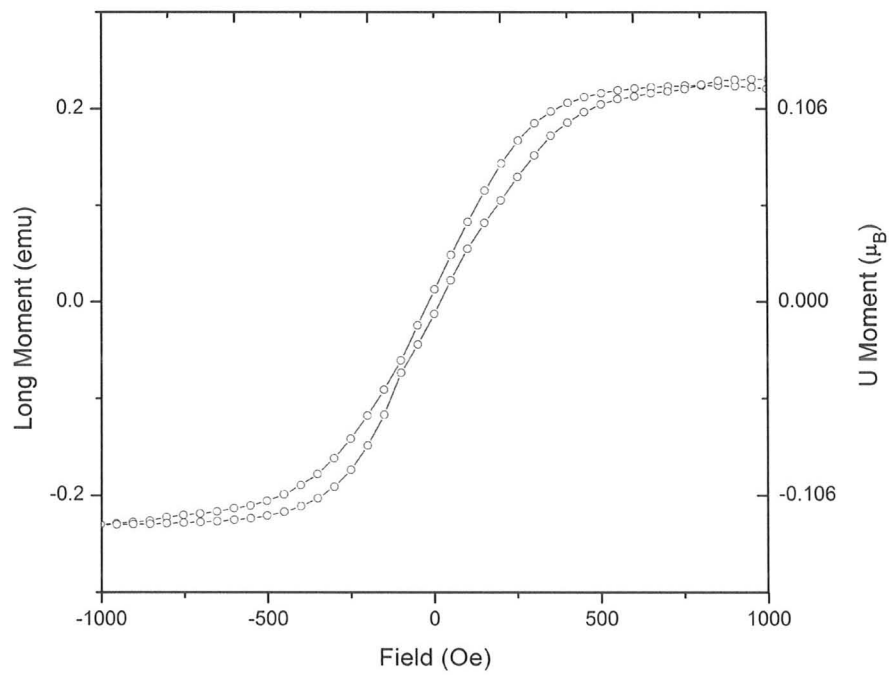

Figure 5.11. Hysteresis loop of the URhGe crystal at T=1.7K. The sample is shown to be magnetically ordered, since hysteresis is present at this temperature. This is expected from the susceptibility measurements.

The measurements indicate that the material is magnetically ordered at 1.7K, which is expected from the susceptibility measurements shown in Figure 5.10. The loop area is still relatively small, which is related to the moment size of $m_0 = 0.37\mu_B$ found in the susceptibility measurements. However, the magnetization is larger here than in the case of UCoGe, since the moment size of URhGe is larger.

5.4 μSR

All of the μSR measurements on URhGe were performed on the sample from the second growth. The measurements concentrated on Zero-Field (ZF)-μSR, but some weak Transverse-Field (TF) measurements were also collected.

The sample was measured in ZF, in a He-4 cryostat, with a base temperature of 1.7K. The ZF- μSR spectra at 1.8K and 10.5K is shown in Figure 5.12. The *y*-axis is the asymmetry between the counters above (Up) and below (Down) the sample, calculated using Equation (3.11). Measuring the asymmetry accounts for the muon decay, such that a perfectly paramagnetic material should have $A(t)$ equal to a constant (ideally zero).

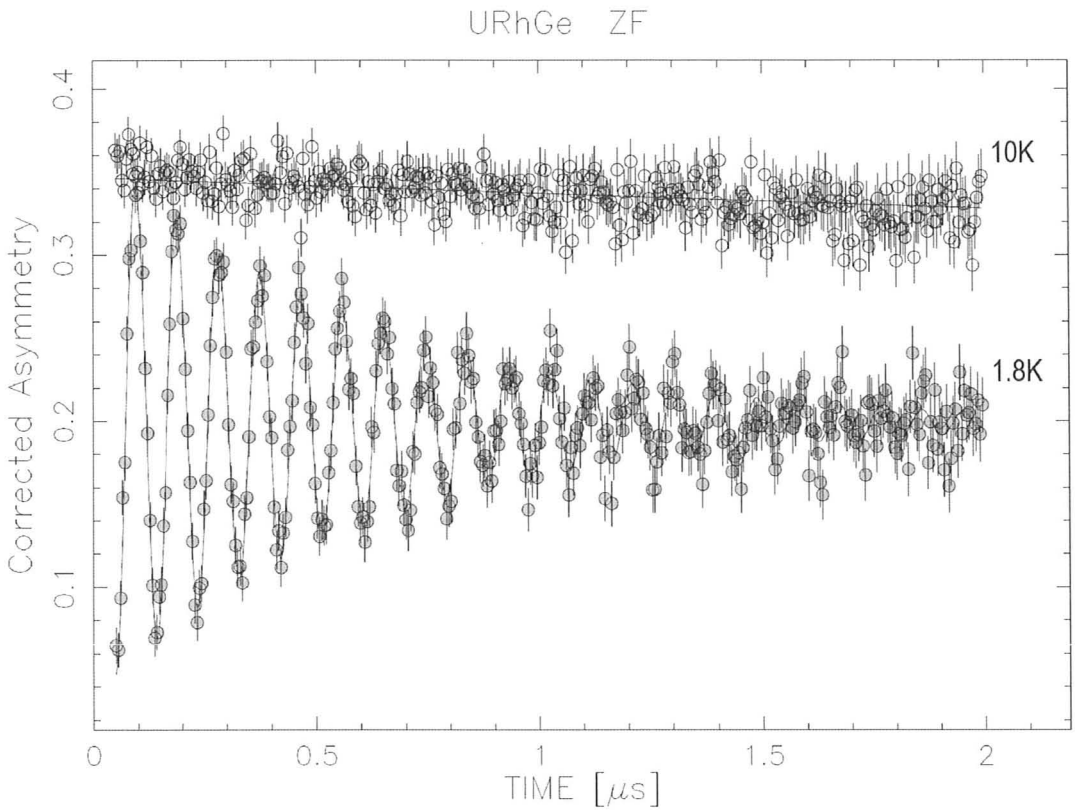

Figure 5.12. ZF-μSR spectra of the URhGe crystal at 10.5K and 1.8K. The spectrum at 10.5K is characteristic of paramagnetic behaviour, while the spectrum at 1.8K is indicative that the sample is in the ferromagnetic state.

The higher temperature measurement displays no precession, which we expect since the sample is in the paramagnetic state. Below 9.5K, the sample is a ferromagnet, so the spectrum at 1.8K displays a precession of the muon spin caused by the local field within the sample. The amplitude of the oscillation decays with time, but can be observed out to a time of at least 1.5μs. The decay of the signal is called the "relaxation" and is observed in nearly all μSR measurements. This relaxation occurs due to a coupling between the muon spin and the magnetic moments in the sample, causing the muon spin to flip. At long times, many muons have undergone this process, and there is a loss of the muon spin coherence.

The ZF-μSR data is fit to the function,

$$A(t)=A_1\exp(-\Lambda t)\cos(\omega t+\theta)+A_2\exp(-\lambda t) \qquad (5.3)$$

where Λ is the relaxation rate of the precessing part of the signal, λ is the relaxation rate of the non-relaxing component, ω is the frequency of the oscillation and θ is the phase of the muon spin polarization. A_1 and A_2 are the asymmetry values for the oscillating and non-oscillating components, respectively. From Equations (3.10) and (3.11), it is apparent that the background, $B_{U,D}$, and the counter asymmetry factor, α, need to be included in the fit. These, in fact, can be fixed by performing a TF-μSR experiment using a weak applied field, and fitting the data to obtain these values. From this weak TF-μSR experiment, we can also find the total asymmetry, A_{tot}, which must be the same for all runs.

By fixing $B_{U,D}$ and α, and stipulating that $A_1 + A_2 = A_{tot}$, there are five free parameters remaining to which to fit each run. Equation (5.3) can be used to fit to the data above the ferromagnetic transition, where it is assumed that $A_1 = 0$ to remove the oscillations. The functional form is now a simple exponential decay, which is expected in the paramagnetic temperature region. A plot of the fit to the ZF-μSR spectrum at 60mK is shown in Figure 5.13. The agreement of this fit is very good, with a reduced $\chi^2 = 1.235$. Fitting the rest of the temperatures below 1.8K with this model gives similarly good agreement, while the temperatures above 1.8K show better agreement.

As previously discussed, the frequency of the precession, ω, is a measure of the local magnetic field at the muon site. In the case of the ferromagnet being studied here, this measures the strength of the field in the material with no applied field. Plotting the frequency versus temperature, we obtain the plot in Figure 5.14.

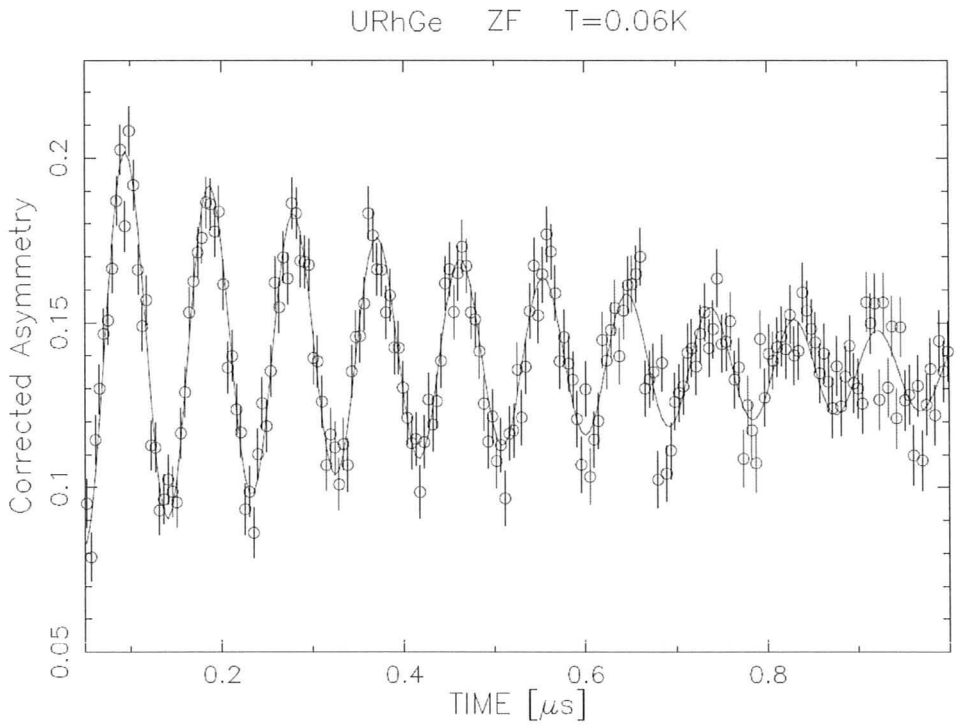

Figure 5.13. ZF-μSR spectrum of the URhGe crystal at 60mK. The solid line shows the fit to the data given by Equation (5.3). The fit to this spectrum had a reduced $\chi^2 = 1.235$, which was typical of runs below 1.8K.

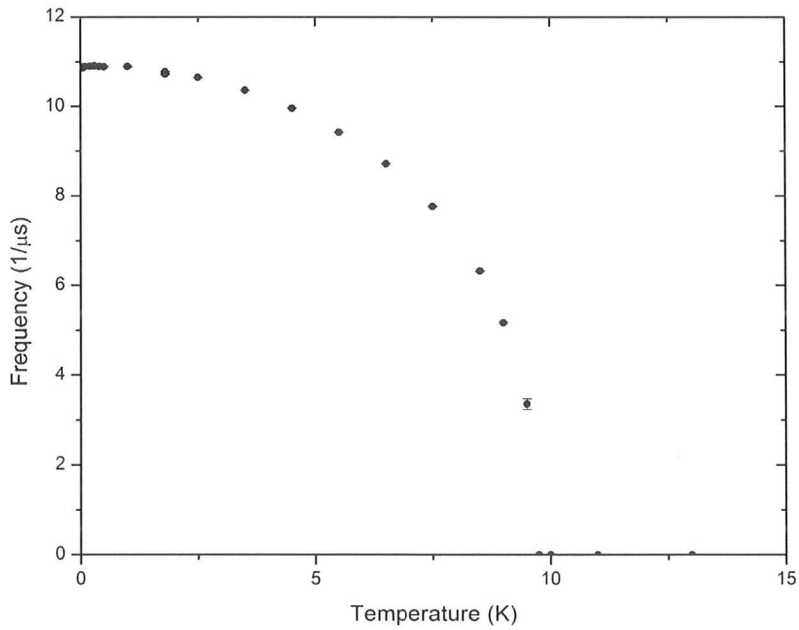

Figure 5.14. Frequency of the μSR signal fit using Equation (5.3). This clearly shows no precession above $T_{Curie} = 9.5K$. The frequency increases toward T = 0K, and shows no change at low T.

Since there is no observed precession above T_{curie}, this could be built into the fits. This leads to a sharp transition at 9.5K, where the precession appears. This corresponds to an abrupt peak in the specific heat observed by other studies [69, 70]. The internal field saturates as $T \rightarrow 0$. Using Equation (3.8), we see that,

$$H_{loc} = \omega / 135.54 \frac{MHz}{T} \qquad (5.4)$$

Since ω = 10.9 MHz as $T \rightarrow 0$, we find that H_{loc} = 0.08 T at the muon site. A muon site for the UCoGe case was derived in [54]. Using a similar approach, the moment size of the U atoms in this system are calculated to be $m_0 = 0.38\mu_B$. This is in excellent agreement with the value of $0.37\mu_B$ found by the susceptibility measurements.

The URhGe crystal was measured in ZF, using a dilution refrigerator with a base temperature of 15mK. The low temperature plot of frequency versus temperature is shown in Figure 5.15.

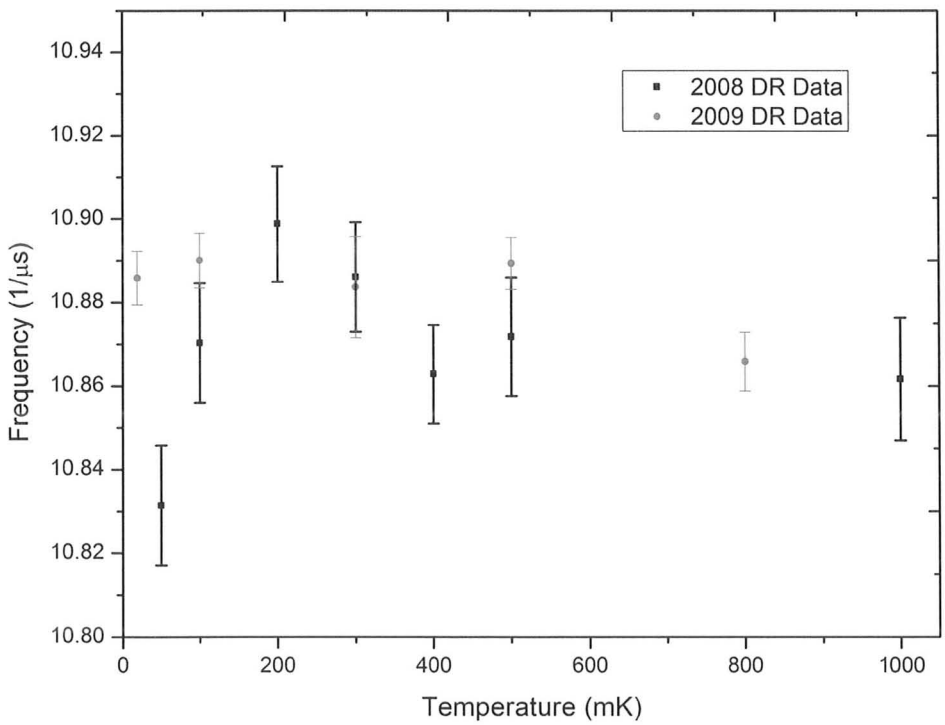

Figure 5.15. Low temperature frequency of the ZF-μSR signal. The black points are those measured in a 2008 study, while the red points were values that were done in 2009 to check the behaviour. No noticeable changes occur at low T. Note the expanded vertical scale.

There is no noticeable change is the frequency at low temperature. Since the samples were shown not to be superconducting, this is not surprising. A 2% drop in the frequency has been reported below T_{sc} for a sample of UCoGe [54]. This is explained by conduction electrons that become superconducting carriers below T_{sc} and no longer contribute a magnetic moment to the system, thereby reducing the magnetic field within the sample. It is unknown if URhGe shows a similar change, and the magnitude of any change compared to UCoGe is also unknown at this time. In the future, repeating these measurements with a superconducting sample of URhGe would be useful in addressing this question.

5.5 Conclusions

The structure characterization measurements have shown that two crystals of URhGe have been prepared. By performing powder X-ray diffraction, it has been shown that these samples compare extremely well to a proposed reference pattern of the material [51]. The powder pattern suggests some impurities, on the order of 5% by volume, which are consistent with elemental Uranium. The Laue pattern shows that the second growth was of better quality than the first, so the remainder of the measurements were performed on the second sample.

SEM measurements were performed to characterize an impurity phase on the surface of the crystal. This impurity consisted of U and Ge in approximately equal amounts. It was approximately 1-2μm thick, contributing less that 1% of the sample volume.

Resistivity measurements show a clear signature of the ferromagnetic transition at 9.5K, which was confirmed with SQUID measurements. A hysteresis loop at 1.7K also showed that the material was

magnetically ordered. The resistivity showed that the material was not superconducting down to 0.02K. This is likely due to sample quality, since our samples showed a smaller RRR value than those reported elsewhere.

The magnetometry measurements were consistent with a Uranium moment size of $m_0 = 0.37\mu_B$ at low temperature. This is in nearly perfect agreement with the moment size of $m_0 = 0.38\mu_B$ measured by ZF-μSR. It is also relatively close to the values reported in the literature [35, 38, 39, 41, 44].

ZF-μSR measurements determined the ferromagnetic transition at 9.5K, showing up as a first order transition. The frequency of the ZF-μSR spectrum saturated at 10.9MHz toward T = 0K. TF-μSR measurements also did not provide any evidence for superconductivity, which was explained by the lack of a superconducting transition in the resistivity data. The other difficulty with measuring the superconducting properties of URhGe by μSR is that it may have a small volume fraction, such as has been reported for UCoGe [54]. To date, we are not aware of any measurements of the superconducting volume fraction in URhGe. In the future, we plan to measure the volume fraction on a superconducting sample of URhGe.

VI. Conclusions

6.1 Structure Characterization

The structure characterization measurements show very good agreement between UCoGe and URhGe. Laue diffraction measurements show that all samples are polycrystalline, but some samples show grains that are more closely aligned. The Laue measurements seem to provide fairly good agreement with the other measurements of the crystal quality. For example, the residual resistivities of the second growths for both samples are larger than for the first growths, and the Laue patterns confirm that the second growths are of better quality.

This trend continues when comparing the materials, where the Laue pattern of the second URhGe growth appeared better than the first UCoGe growth, but not as closely aligned as in the second UCoGe sample. The resistivity measurements appear to support this measure of the crystal quality. This will be discussed further in Section 6.2.

We notice that the powder X-ray diffraction patterns for both materials display a prominent impurity peak around $2\theta = 36°$. This indicates that it is most likely due to a common impurity. The most likely candidate for this impurity is elemental Uranium, since the α-Uranium phase shows several strong peaks around this scattering angle. Considering the results of the SEM measurements on URhGe, the other possibility is that the impurity phase is due to UGe or a material of similar stoichiometry. However, the SEM measurements showed the level of this surface impurity to be ~1%, which is lower than the level measured by powder X-ray diffraction. This remains an issue that can be addressed in further growths of

these materials.

6.2 DC Resistivity

The resistivity measurements on UCoGe show no change at T_{Curie}, which is due to the small moments in the material. Disagreements exist as to whether the ferromagnetic transition can be seen in resistivity, with some claiming to see a change in the slope [48, 66], and others not [46, 54]. Both of these references had a crystal with *RRR* = 30. In the future, with better quality crystals, it may be possible to address this question.

The second UCoGe crystal showed a clear superconducting transition, with an onset of $T_{SC\ onset}$ = 425mK, and zero resistance at $T_{SC\ \rho=0}$ = 300mK. The broadness of this peak is typical in this material, and has been reported to be of similar size elsewhere [54]. These values will be used for other low temperature measurements to look for possible changes in the superconducting state.

Resistivity measurements performed on the URhGe samples displayed a signature of the ferromagnetic transition at 9.5K in URhGe, but no superconducting transition. From Figure 5.8, we can calculate *RRR* $\approx$ 10, which is slightly lower than reported elsewhere. The lack of superconductivity in this sample means that other measurements collected in this regime will not show any effects that would be attributed to superconductivity.

6.3 Bulk Magnetometry

The magnetization measurements show that both materials undergo a magnetic transition. The transition is much sharper in URhGe as compared to UCoGe. This is likely due to the moment size in the two materials. Since URhGe has a larger ordered moment, the magnetization of the sample is larger, compared to UCoGe.

Similarly weak signals of the ferromagnetic transition in UCoGe have been observed previously[45, 48, 66]. This signal does not seem to become sharper with increased sample quality, so it is unlikely that this effect is due to impurities in the sample. This has lead to some disagreement about the exact value of T_{Curie} in this system, with values claimed to be in the range of 1.5K to 3.5K [39, 45, 46, 48]. The measurements reported here, in being similar to other measurements of this material, do not clarify the transition. Rather, they continue to show that the transition is broad in temperature.

The difference between the ferromagnetic properties of the two systems is also evident when comparing the hysteresis curves at 1.7K, Figures 4.9 and 5.11. The magnetization of the URhGe sample is larger, and the hysteresis loop is more open. This indicates stronger magnetic ordering, due to its larger moment.

The moment sizes of $0.37\mu_B$ and $0.05\mu_B$ found by the magnetization measurements in this study are on the order of those reported elsewhere [39, 45, 46, 48]. Some of the reported values are higher than those found here, which may be due to impurities in the system.

6.4 μSR

The ZF-μSR measurements on both UCoGe and URhGe showed clear ferromagnetic transitions. The transition was very sharp in URhGe, while being slightly broadened for UCoGe. This is consistent with both the magnetization measurements, which showed a broad transition for UCoGe and a sharp transition of URhGe, and with other data presented in the literature [35, 39, 42, 45, 48]. The behaviour of both materials was the same, with the frequency tending toward a constant value at low temperatures. This frequency at T = 0K, along with calculations of the muon site [54], allowed the calculation of the size of the magnetic moments in the system. The values, $0.38\mu_B$ and $0.065\mu_B$, are in excellent agreement with the magnetization measurements.

The URhGe crystal is not superconducting, so consequently displayed no changes at low temperatures that would indicate a superconducting transition. The UCoGe crystal did show a sharp decrease in the frequency between 0.3 and 0.5K of ~10%. This behaviour agrees with other μSR measurements in the superconducting state of UCoGe, though the decrease shown by our sample is larger than has been reported elsewhere [54]. The most likely reason for this disagreement is due to possible differences in the fitting procedure.

Since the sample is superconducting, TF-μSR measurements were performed on UCoGe, down to 0.02K, in fields up to 1T. These measurements did not show any evidence for the superconducting transition, and so could not be used to measure any of the superconducting properties of UCoGe with reasonable confidence.

6.5 Conclusions

This work comprises a thorough study of UCoGe and URhGe at ambient pressure. The materials we have grown both displayed ferromagnetic transitions that were measured by magnetometry and ZF-μSR, and found to agree very well. The U magnetic moment measured by these two techniques were also found to be nearly identical.

Resistivity measurements on URhGe showed that our sample was not superconducting down to 0.02K. The second growth of UCoGe was found to be superconducting below 300mK, which was also confirmed by ZF-μSR measurements. However, due to the small volume fraction, TF-μSR measurements could not extract reliable values for the superconducting properties of UCoGe.

Other crystal growths had been performed that produced good quality samples of both materials. However, these crystals were destroyed during the annealing process. Future efforts will include modifying the annealing procedure to avoid damaging the crystals. We have obtained high-purity Uranium from Ames Laboratory, which has been purified by electromigration. This will be used in future growths to hopefully improve the *RRR*.

In the future, efforts will be continued to refine the crystal growth technique to produce higher quality samples of both UCoGe and URhGe. The goal for these growths is also to produce crystals that are both ferromagnetic and superconducting, with transition temperatures as high as most reported in the literature. Following a successful growth with these properties, continued measurements in the superconducting region, including μSR, will be performed to better understand the superconducting properties of these materials.

Other possible projects that can be conducted on these materials in the future involve studies under pressure, in large applied fields, or on intermediate dopings in the U(Rh,Co)Ge series.

References

[1] Z. Fisk, D.W. Hess, C.J. Penthick, D. Pines, J.L. Smith, J.D. Thompson and J.O. Willis. *Science* **239** (1988) 33

[2] K. Kadowaki, and S.B. Woods. *Solid State Comm.* **58** (1986) 507

[3] A. Wasserman, M. Springford, and A.C. Hewson. *J. Phys: Cond. Matt.* **1** (1989) 2669

[4] Z. Fisk, H.R. Ott, T.M. Rice and J.L. Smith. *Nature* **320** (1986) 124

[5] G.R. Stewart. *Rev. Mod. Phys.* **56** (1984) 755

[6] L. Taillefer, R. Newbury, G.G. Lonzarich, Z. Fisk, and J.L. Smith. *J. Magn. Magn. Mater.* **63-64** (1987) 372

[7] J.D. Thompson, Z. Fisk, and H.R. Ott. *J. Magn. Magn. Mater.* **54-57** (1986) 393

[8] M.A. Ruderman and C. Kittel. *Phys. Rev.* **96** (1954) 99

[9] T. Kasuya. *Prog. Theor. Phys.* **16** (1956) 45

[10] K. Yosida. *Phys. Rev.* **106** (1957) 893

[11] J. Kondo. *Prog. Theor. Phys. Jpn.* **32** (1964) 37

[12] R.H. Heffner and M. Norman. *arXiv/cond-mat:*9506043 (1995)

[13] C.J. Penthick and D. Pines. Novel Superconductivity. Plenum Press, New York, 1987. p. 201

[14] S. Doniach. *Physica B* **91** (1977) 213

[15] S. Kambe, H. Sakai, Y. Tokunaga, T. Fujimoto, H. Kato, R.E. Walstedt, S. Ikeda, T.D. Matsuda, Y. Haga and Y. Onuki. *J. Phys. Soc. Jpn.* **75** (2006) 127

[16] S. Kondo, D.C. Johnston, C.A. Swenson, F. Borsa, A.V. Mahajan, L.L. Miller, T.Gu, A.I. Goldman, M.B. Maple, D.A. Gajewski, E.J. Freeman, N.R. Dilley, R.P. Dickey, J. Merrin, K. Kojima, G.M. Luke, Y.J. Uemura, O. Chmaissem and J.D. Jorgensen. *Phys. Rev. Lett.* **78** (1997) 3729

[17] H.H. Hill. Plutonium and Other Actinides. AIME, New York, 1970.

[18] N. Grewe and F. Steglich. Handbook on the Physics and Chemistry of Rare Earths. Elsevier, Amsterdam, 1991. p. 343

[19] H.R. Ott and Z. Fisk. Handbook on the Physics and Chemistry of Actinides. Elsevier, Amsterdam, 1987. p. 85

[20] N.F. Berk and J. R. Schrieffer, *Phys. Rev. Lett.* **17** (1966) 433

[21] G.M. Luke, A. Keren, K. Kojima, L.P. Le, B.J. Sternlieb, W.D. Wu, Y.J Uemura, Y. Ōnuki and T. Komatsubara. *Phys. Rev. Lett.* **73** (1994) 1853

[22] J.L. Sarrao, L.A. Morales, J.D. Thompson, B.L. Scott, G.R. Stewart, F. Wastin, J. Rebizant, P. Boulet, E. Colineau and G.H. Lander. *Nature* **420** (2002) 297

[23] A.A. Abrikosov and L.P. Gor'kov. *Zh. Eksp. Teor. Fiz.* **39** (1960) 1781

[24] A.C. Hewson. The Kondo problem to heavy fermions. Cambridge University Press, Cambridge UK, 1997. p. 16

[25] R.A. Fisher, S. Kim, B.F. Woodfield, N.E. Phillips, L. Taillefer, K. Hasselbach, J. Flouquet, A.L. Giorgi and J.L. Smith. *Phys. Rev. Lett.* **62** (1989) 1411

[26] G. Bruls, D. Weber, B. Wolf, P. Thalmeier, B. Luthi, A. de Visser and A. Menovsky. *Phys. Rev. Lett.* **65** (1990) 2294

[27] A. Adenwalla, S.W. Lin, Q.Z. Ran, Z. Zhao, J.B. Ketterson, J.A. Sauls, L. Taillefer, D.G. Hinks, M. Levy and B.K. Sarma. *Phys. Rev. Lett.* **65** (1990) 2298

[28] G.M. Luke, A. Deren, L.P. Le, W.D. Wu, Y.J. Uemura, D.A. Bonn, L. Taillefer and J.D. Garrett. *Phys. Rev. Lett.* **71** (1993) 146

[29] C. Broholm, G. Aeppli, R.N. Kleiman, D.R. Harshman, D.J. Bishop, E. Bucher, D.Ll. Williams, E.J. Ansaldo and R.H. Heffner. *Phys. Rev. Lett.* **65** (1990) 2062

[30] B.S. Shivram, Y.H. Jeong, T.F. Rosenbaum and D.G. Hinks. *Phys. Rev. Lett.* **56** (1986) 1078

[31] A. Huxley, I. Sheikin, E. Ressouche, N. Kernavanois, D. Braithwaite, R. Calemmczuk, and J. Flouquet. *Phys. Rev. B* **63** (2001) 144519

[32] S.S. Saxena, P. Argarwal, K. Ahilan, F. M. Grosche, R. K. W. Haselwimmer, M. J. Steiner, E. Pugh, I. R. Walker, S. R. Julian, P. Monthoux, G. G. Lonzarich, A. Huxley, I. Sheikin, D. Braithwaite and J. Flouquet. *Nature* **406** (2000) 587

[33] G. Oomi, T. Kageyama, K. Nishimura, S. W. Yun, Y. Onuki: *Physica B* **206** (1995) 515

[34] A. Harada, S. Kawasaki, H. Kotegawa, Y. Kitaoka, Y. Haga, E. Yamamoto, Y. Ōnuki, K.M. Itoh, E.E. Haller and H. Harima. *J. Phys. Soc. Jpn.* **74** (2005) 2675

[35] D. Aoki, A. Huxley, E. Ressouche, I. Sheikin, J. Flouquet, J.P. Brison, and C. Paulsen: *J. Phys. Chem. Solids* **63** (2002) 1179

[36] E.A. Knetsch, A.A. Menovsky, G.J. Nieuwenhuys, J.A. Mydosh, A. Amato, R. Feyerherm, F.N. Gygax, A. Schenck, R.H. Heffner and D.E. MacLaughlin. *Physica B* **186-188** (1993) 300

[37] A. Amato, C. Geibel, F.N. Gygax, R.H. Heffner, E. Knetsch, D.E. MacLaughlin, C. Schank, A. Schenck, F. Steglich and M. Weber. *Z. Phys. B* **86** (1992) 159

[38] D. Aoki, A. Huxley, E. Ressouche, D. Braithwaite, J. Flouquet, J.-P. Brison, E. Lhotel and C. Paulsen. *Nature* **413** (2001) 613

[39] F. Lévy, I. Sheikin, B. Grenier and A.D. Huxley. *Science* **309** (2005) 1343

[40] K. Oikawa, T. Kamiyama, H. Asano, Y. Ōnuki and M. Kohgi. *J. Phys. Soc. Jpn.* **65** (1996) 3229

[41] F. Hardy, A. Huxley, J. Flouquet, B. Salce, G. Knebel, D. Braithwaite, D. Aoki, M. Uhlarz, and C. Pfleiderer: *Physica B* **359** (2005) 1111

[42] A. Miyake, D. Aoki, and J. Flouquet. *arXiv/cond-mat:*0905.2225 (2009)

[43] F. Lévy, I. Sheikin, B. Grenier, C. Marcenat and A.D. Huxley. *J. Phys.: Cond. Matt.* **21** (2009)

164211

[44] A. Miyake, D. Aoki, and J. Flouquet. *J. Phys. Soc. Jpn.* **77** (2008) 094709

[45] N.T. Huy, D.E. de Nijs, Y.K. Huang, and A. de Visser. *Phys. Rev. Lett.* **99** (2007) 067006

[46] E. Hassinger, D. Aoki, G. Knebel and J. Flouquet. *arXiv/cond-mat:*0804.0500v1 (2008)

[47] T. Ohta, Y. Nakai, Y. Ihara, K. Ishida, K. Deguchi, N.K. Sato and I. Satoh. *J. Phys. Soc. Jpn.* 77 (2008) 023707

[48] N.T. Huy, D.E. de Nijs, Y.K. Huang, and A. de Visser. *Phys. Rev. Lett.* **100** (2008) 077001

[49] V.P. Mineev. *Phys. Rev. B* **66** (2002) 134504

[50] N.V. Abrosimov, S.N. Rossolenko, V. Alex, A. Gerhardt and W. Schöder. *J. Crys. Growth.* **166** (1996) 657

[51] F. Canepa, P. Manfrinetti, M. Pani, and A. Palenzona. *J. All. Comp.* **234** (1996) 225

[52] F. Hardy and A. Huxley. *Phys. Rev. Lett.* **94** (2005) 247006

[53] J. Poltierová Vejpravová, J. Pospíšil and V. Sechovský. *arXiv/cond-mat:*0806.3561 (2008)

[54] A. de Visser, N.T. Huy, A. Gasparini, D.E. De Nijs, D. Andreica, C. Baines, and A. Amato. *Phys. Rev. Lett.* **102** (2009) 167003

[55] S.R. Andrews and R.A. Cowley. *J. Phys. C: Solid State Phys.* **18** (1985) 6427

[56] J.I. Langford and D. Louër. *Rep. Prog. Phys.* **59** (1996) 131

[57] C. Kittel. Introduction to Solid State Physics. 7th Ed. John Wiley and Sons Inc., New York, NY, 1996.

[58] N.W. Ashcroft and N.D. Mermin. Solid State Physics. Harcourt College Publishers, Orlando, FL, 1976. p. 699-700.

[59] G.J. MacDougall. *Ph.D. Thesis*. McMaster University, 2008.

[60] M. Tinkham. Introduction to Superconductivity. 2nd Ed. McGraw Hill Inc., Whitby, ON, 1996.

[61] S.N. Erné, H.-D. Hahlbohm and H. Lübbig. *J. Appl. Phys.* **47** (1976) 5440

[62] E. Du Trémolete de Lacheisserie, D. Gignoux and M. Schlenker. Magnetism: Materials and Applications. Vol. 2. Springer, New York, NY, 2005.

[63] A. Schenck. Muon Spin Rotation Spectroscopy: Principles and Applications in Solid State Physics. Adam Hilger Ltd., Bristol and Boston, 1985

[64] T. Le Bihan, S. Heathman, M. Idiri, G.H. Lander, J.M. Wills, A.C. Lawson and A. Lindbaum. *Phys. Rev. B* **67** (2003) 134102

[65] G.H. Lander, E.S. Fisher and S.D. Bader. *Adv. Phys.* **43** (1994) 1

[66] N.T. Huy, Y.K. Huang and A. De Visser. *J. Mag. Mag. Mat.* **321** (2009) 2691

[67] E. Della Torre. Magnetic Hysteresis. IEEE Computer Society Press, 2000.

[68] J.W. Ross and D.J. Lam. *Phys. Rev.* **165** (1968) 617

[69] S. Sakarya, N.H. van Dijk, A. de Visser and E. Brück. *Phys. Rev. B* **67** (2003) 144407

[70] K.H.J. Buschow, E. Brück, R.G. van Wierst, R.F. de Boer, L. Havela, V. Sechovsky, P. Nozar, E. Segiura, M. Ono, M. Date and A. Yamagishi. *J. Appl. Phys.* **67** (1990) 5215

[71] A.J. Freeman and G.H. Lander. Handbook on the physics and chemistry of the actinides. Elsevier, Amsterdam, 1984.